SPRINGER BRIEFS IN MOLECULAR SCIENCE
ULTRASOUND AND SONOCHEMISTRY

Kenji Okitsu · Francesca Cavalieri

Sonochemical Production of Nanomaterials

Springer

SpringerBriefs in Molecular Science

Ultrasound and Sonochemistry

SpringerBriefs in Molecular Science: Ultrasound and Sonochemistry is a series of concise briefs that present those interested in this broad and multidisciplinary field with the most recent advances in a broad array of topics. Each volume compiles information that has thus far been scattered in many different sources into a single, concise title, making each edition a useful reference for industry professionals, researchers, and graduate students, especially those starting in a new topic of research.

More information about this series at http://www.springer.com/series/15634

About the Series Editors

Bruno G. Pollet is a full Professor of Renewable Energy at the Norwegian University of Science and Technology (NTNU) in Trondheim. He is a Fellow of the *Royal Society of Chemistry* (RSC), an Executive Editor of *Ultrasonics Soncohemistry* and a Board of Directors' member of the *International Association of Hydrogen Energy* (IAHE). He held Visiting Professorships at the University of Ulster, Professor Molkov's HySAFER (UK) and at the University of Yamanashi, Professor Watanabe's labs (Japan). His research covers a wide range of areas in Electrochemical Engineering, Electrochemical Energy Conversion and Sono-electrochemistry (Power Ultrasound in Electrochemistry) from the development of novel materials, hydrogen and fuel cell to water treatment/disinfection demonstrators & prototypes. He was a full Professor of Energy Materials and Systems at the University of the Western Cape (South Africa) and R&D Director of the National Hydrogen South Africa (HySA) Systems Competence Centre. He was also a Research Fellow and Lecturer in Chemical Engineering at The University of Birmingham (UK) as well as a co-founder and an Associate Director of The University of Birmingham Centre for Hydrogen and Fuel Cell Research. He has worked for Johnson Matthey Fuel Cells Ltd (UK) and other various industries worldwide as Technical Account Manager, Project Manager, Research Manager, R&D Director, Head of R&D and Chief Technology Officer. He was awarded a Diploma in Chemistry and Material Sciences from the Université Joseph Fourier (Grenoble, France), a B.Sc. (Hons) in Applied Chemistry from Coventry University (UK) and an M.Sc. in Analytical Chemistry from The University of Aberdeen (UK). He also gained his Ph.D. in Physical Chemistry in the field of Electrochemistry and Sonochemistry under the supervision of Profs. J. Phil Lorimer & Tim J. Mason at the Sonochemistry Centre of Excellence, Coventry University (UK). He undertook his PostDoc in Electrocatalysis at the Liverpool University Electrochemistry group led by Prof. David J. Schiffrin. Bruno has published many scientific publications, articles, book chapters and books in the field of Sonoelectrochemistry, Fuel Cells, Electrocatalysis and Electrochemical Engineering. Bruno is member of editorial board journals (*International Journal of Hydrogen Energy*/*Electrocatalysis*/*Ultrasonics Sonochemistry*/*Renewables-Wind, Water and Solar*/*Electrochem*). He is also fluent in English, French and Spanish. *Current Editorships: Hydrogen Energy and Fuel Cells Primers Series (AP, Elsevier)* and *Ultrasound and Sonochemistry (Springer)*.

Prof. Muthupandian Ashokkumar (Ashok) is a Physical Chemist who specializes in Sonochemistry, teaches undergraduate and postgraduate Chemistry and is a senior academic staff member of the School of Chemistry, University of Melbourne. Ashok is a renowned sonochemist, with more than 20 years of experience in this field, and has developed a number of novel techniques to characterize acoustic cavitation bubbles and has made major contributions of applied sonochemistry to the Materials, Food and Dairy industry. His research team has developed a novel ultrasonic processing technology for improving the functional properties of dairy ingredients. Recent research also involves the ultrasonic synthesis of functional nano- and biomaterials that can be used in energy production, environmental remediation and diagnostic and therapeutic medicine. He is the Deputy Director of an Australian Research Council Funded Industry Transformation Research Hub (ITRH; http://foodvaluechain.unimelb.edu.au/#research; Industry Partner: Mondelez International) and leading the Encapsulation project (http://foodvaluechain.unimelb.edu.au/research/ultrasonic-encapsulation). He has received about $ 15 million research grants to support his research work that includes several industry projects. He is the Editor-in-Chief of *Ultrasonics Sonochemistry*, an international journal devoted to sonochemistry research with a Journal Impact Factor of 4.3). He has edited/co-edited several books and special issues for journals; published ~360 refereed papers (H-Index: 49) in high impact international journals and books; and delivered over 150 invited/keynote/plenary lectures at international conferences and academic institutions. Ashok has successfully organised 10 national/international scientific conferences/workshops and managed a number of national and international competitive research grants. He has served on a number of University of Melbourne management committees and scientific advisory boards of external scientific organizations. Ashok is the recipient of several prizes, awards and fellowships, including the Grimwade Prize in Industrial Chemistry. He is a Fellow of the RACI since 2007.

Kenji Okitsu · Francesca Cavalieri

Sonochemical Production of Nanomaterials

With Contributions by Sukhvir Kaur Bhangu,
Enrico Colombo and Muthupandian Ashokkumar

Springer

Kenji Okitsu
Graduate School of Humanities
and Sustainable System Sciences
Osaka Prefecture University
Osaka, Japan

Francesca Cavalieri
Department of Chemical Engineering
The University of Melbourne
Parkville, VIC, Australia

ISSN 2191-5407 ISSN 2191-5415 (electronic)
SpringerBriefs in Molecular Science
ISSN 2511-123X ISSN 2511-1248 (electronic)
Ultrasound and Sonochemistry
ISBN 978-3-319-96733-2 ISBN 978-3-319-96734-9 (eBook)
https://doi.org/10.1007/978-3-319-96734-9

Library of Congress Control Number: 2018948686

This Springer imprint is published by the registered company Springer Nature Switzerland AG
The registered company address is: Gewerbestrasse 11, 6330 Cham, Switzerland

Contents

Chapter 1
Chemical and Physical Effects of Acoustic Bubbles

Abstract During acoustic cavitation which comprises sequence of nucleation, growth, and collapse of bubbles, physical effects due to shockwaves, micro-jets, strong micro-stirring, etc. are produced. In addition, when bubbles were adiabatically collapsed, the temperature and pressure in collapsing bubbles attained extreme high temperature and high pressure which cause high-temperature reactions in gas and/or liquid phases of the bubble interface. Various types of radicals are also formed by the pyrolysis of solutes and/or solvents. In this chapter, chemical and physical effects of acoustic cavitation are introduced to understand characteristics of the bubbles formed.

Keywords High temperature · High pressure · Pyrolysis · Radical reaction
Shockwave · Micro-jet · Strong micro-stirring

Ultrasound is defined as sound more than 20 kHz, and human beings are not audible ultrasound. Since sound wave consists of rarefaction and compression cycle, ultrasound irradiation of a liquid leads to the generation of cavitation which comprises sequence of nucleation, growth, and collapse of bubbles. This is referred to as acoustic cavitation. As a similar phenomenon, the term hydrodynamic cavitation is used when a turbulent flow of a fluid is produced by high-speed screw rotation or high-flow rate of a fluid in a pipe. During acoustic cavitation, the formation of shockwaves, micro-jets, micro-stirring, etc. are produced. These phenomena are classified as physical effects (or mechanical effects). Ultrasound itself and physical effects described above cannot directly excite any atoms and molecules. However, for example, in the case of a heterogeneous solution including a solid metal reagent, shockwaves and micro-jets can physically activate the metal reagent to remove an inactive part on the reagent surface and to enhance the mass transfer of solutes to the reagent, resulting in the acceleration of the reactions on the reagent.

In addition to above phenomena, when bubbles were adiabatically collapsed, the temperature and pressure in collapsing bubbles attained extreme high temperature and high pressure. The bubbles with high temperature cause high-temperature reactions in gas and/or liquid phases of the bubble interface. As a result, various types of radicals are formed by the pyrolysis of solutes and/or solvents so that a

K. Okitsu et al., *Sonochemical Production of Nanomaterials*,
Ultrasound and Sonochemistry, https://doi.org/10.1007/978-3-319-96734-9_1

number of radical reactions are induced. Therefore, acoustic cavitation provides unique chemical effects and reaction fields in addition to physical effects.

Chemistry and the reaction related to above phenomena are referred to as "sonochemistry" and "sonochemical reaction" or "sonolysis". Because of extreme high temperature in a collapsing bubble, light is emitted from the bubble due to excited chemical species, black body, and/or plasma. This phenomenon is referred to as "sonoluminescence". Unique phenomena induced by acoustic cavitation are studied actively in the field of chemistry, physics, biology, medical sciences as well as environmental technology and nanotechnology. Sonochemistry is attracted much attention for the synthesis of functional nanoparticles and nanostructured materials, because unique phenomena and extreme high-temperature reaction conditions can be easily produced in the solution. In this chapter, let us study the characteristics of acoustic cavitation bubbles (acoustic bubbles), which will help to understand how to apply ultrasound and acoustic bubbles in nanomaterial syntheses.

1.1 Characteristics of Acoustic Bubbles

When ultrasound is irradiated to a liquid, the formation of bubble nuclei originated from dissolved gases, their growth, and collapse of bubbles occurs. When bubbles are driven into an implosive collapse adiabatically, localized high temperatures and pressures are produced in collapsing bubbles. Depending on the irradiation system, the transient bubbles (lifetime from nucleation to collapse of a bubble is about μs order which corresponding to the passing ultrasound consisting of one or several rarefaction and compression cycles of ultrasound) or stable bubbles (lifetime is about ms order) are formed. Tronson et al. reported that, in a condition, 20 kHz ultrasound produces transient bubbles, but 515 kHz ultrasound produces stable bubbles [1].

Ambient radius for an active bubble is defined as the radius of bubble which starts Rayleigh collapse. The experimentally observed ambient radius for an active bubble is reported to be 3–6 μm at 27 kHz and 0.3–0.6 μm at 1 MHz [2]. The size of an active bubble is in the range from Blake threshold radius (lower bound) to linear resonance radius (upper bound) [3]. The details are described in [4].

The maximum temperature, $T_{\max}$, reached in a collapsing bubble can be theoretically determined as

$$T_{max} = \frac{T_0 P_{max}(\gamma - 1)}{P_0} \tag{1.1}$$

where T_0 is the temperature of the sample solution, $P_{\max}$ is the maximal pressure at the moment of bubble collapse, γ is the specific heat ratio (C_p/C_v), and P_0 is the sum of the vapor pressures of the solvent and the dissolved gas pressure [5].

From Eq. (1.1), it is clear that the important factor affecting $T_{\max}$ is the γ value of a dissolved gas. For example, the γ value (at 300 K and 1 atm) of gas changes as 1.293 for CO_2, 1.401 for N_2, 1.670 for Ar [6]. More information is listed in Table 1.1.

Table 1.1 Physical properties of various gases

Gas	Specific heats ratio, γ [11] (at 1 atm)	Thermal conductivity, λ (10^{-4}W/mK) [12] (at 300 K and 1 atm)	Gas solubility in water, (ratio of mol fraction) [13] (at 25 °C and 1 atm)
He	1.63 (−180 °C)	1510	0.0700×10^{-4}
Ne	1.64 (19 °C)	493	0.0815×10^{-4}
Ar	1.668 (15 °C)	178.7	0.252×10^{-4}
Kr	1.68 (19 °C)	94.2	0.451×10^{-4}
Xe	1.66 (19 °C)	56.2	0.788×10^{-4}
O_2	1.401 (15 °C)	267.4	0.229×10^{-4}
N_2	1.404 (15 °C)	259	0.118×10^{-4}
CO_2	1.304 (15 °C)	166.2	6.10×10^{-4}
CH_4	1.31 (10 °C)	343	0.253×10^{-4}
H_2O	1.324 (100 °C)	181	
CH_3OH	1.203 (77 °C)	143	
C_6H_{14} (hexane)	1.08 (80 °C)	128	

When the dissolved gas has higher γ value, the temperature attained upon bubble collapse becomes higher. Furthermore, the solvent vapor affects T_{max}. It should be noted that γ of the solvent vapor tends to have lower γ value compared with those of one- and two-atomic gases. Therefore, to produce bubbles with high T_{max}, one has to pay attention to the γ value of the solvent vapor.

Equation (1.1) obtained theoretically cannot show the exact temperatures and pressures attained in the real collapsed bubble, because various other parameters such as thermal conductivity of gas, surface tension and viscosity of solvent, external hydrostatic pressure, etc. will affect acoustic cavitation [7, 8]. Physical properties of gases such as specific heats ratio, thermal conductivity, and solubility in water are listed in Table 1.1. For example, acoustic cavitation consisting of a dissolved gas with higher thermal conductivity will result in the formation of less adiabatically collapsed bubbles, resulting in the suppression of the increase in the temperature during collapsing bubbles: T_{max} attained will become lower when the dissolved gas with higher thermal conductivity was used. The solubility of a dissolved gas is also the important parameters. For example, acoustic cavitation consisting of a dissolved gas with higher solubility in water will result in the formation of a larger number of bubbles. The amount of gas in a liquid affects the number of high-temperature bubbles formed [9, 10].

The temperature and pressure attained in collapsed bubbles are important to apply acoustic cavitation to various chemical reactions. Table 1.2 shows the bubble temperature and pressure obtained from a calculation and several experiments of acoustic cavitation [7, 14–21], where representative measurement methods have been developed from 1950 to 1996. As shown in Table 1.2, the temperature and pressure of

collapsed bubbles are around 3000–6000 K and 300–1700 atm. Such bubbles are often referred to as "hot-spots" or "hot-spot cavities". The first experimental estimation of the bubble temperature and pressure was carried out in aqueous alkali halide solutions by Sehgal et al., where the emission from excited Na and K atoms was analyzed [7]. In organic and polymeric liquids, Suslick et al. found that the temperatures attained in collapsed bubbles were approximately 5000 K, which were obtained by analyzing the reaction kinetics of the metal–carbonyl complex decomposition rates [14] and the sonoluminescence spectra of excited state of diatomic carbon, C_2, emission [19]. Misik et al. used a semi-classical kinetics model of isotope effect of H and D atoms formed in a sonicated Ar-saturated 1:1 H_2O–D_2O mixture solution and estimated the bubble temperature to be 2000–4000 K [15]. Later, many researchers as Tauber et al. [22], Ashokkumar and Grieser [23], and Okitsu et al. [10] were investigated the bubble temperatures by analyzing the reaction kinetics of methyl radical recombination, where the sonolysis of aqueous *t*-butanol solution was performed to produce methyl radicals. Eddingsaas and Suslick reported that a temperature of collapsing bubbles reached ~8000 K and core of collapsing bubble was in plasma [24], when concentrated sulfuric acid was sonicated directly by using a Ti horn sonicator at 20 kHz under Ar.

The experimentally measured temperatures shown in Table 1.2 are based on multi-bubble cavitation so that the temperature corresponds to the average temperature of a number of collapsing bubbles. Since multi-bubble cavitation still includes complex phenomena arising from the interaction and coalescence of bubbles, the number and distribution of bubble, etc., single-bubble cavitation, and its dynamics are also investigated actively. For example, the maximum temperature attained in collapsing single bubble is generally higher than that in collapsing multi-bubbles. This is because more ideal symmetric collapse of bubble to the smaller bubble size would occur in the case of single bubble so that the bubble collapsing achieves more adiabatically.

The reaction sites of a collapsing bubble consist of three different sites as inside, interface of bubble, and bulk solution. The types of sonochemical reactions can be classified as (i) reactions inside the bubble and its interface region (pyrolysis or combustion reactions), (ii) reactions with active radicals which are formed from pyrolysis of solvent and/or solutes molecules (radical reactions), and (iii) reactions induced by physical effects (shockwaves and micro-jets, micro-stirring, etc.) which are produced upon bubble collapsing. Physical effects result in rapid mass transfer, surface treatment or cleaning of solid, particle size reduction, particle aggregation, depolymerization, etc. The details are also described in Chap. 2.

1.2 Calorimetry for Ultrasound Power Measurement

The nominal electric power of ultrasound apparatus is not the real power of ultrasound irradiated from oscillator. Calorimetry can be used to estimate the real power of ultrasound irradiated to a liquid [25]. When ultrasound is irradiated to water, the

Table 1.2 Temperature and pressure attained in collapsing bubble reported by representative measurement methods

Author (year)	Solvent/atmosphere	Temperature/K	Pressure/atm	Note (references)
Noltingk et al. (1950)	Water/N_2	4200	975	Calculation [16]
Sehgel et al. (1979)	Water/Ar	3360	313	Emission of excited-state alkali metal [7]
Hart et al. (1986)	Water/Ar	4000		comparative rate thermometry (N_2O) [17]
Suslick et al. (1986)		5200 ± 500		comparative rate thermometry (metal$(CO)_x$) [14]
Hart et al. (1990)	Water/Ar	2720		comparative rate thermometry (CH_4) [18]
Suslick et al. (1992)	Silicon oil/Ar	5075 ± 156		Emission of excited-state C_2 [19]
Suslick et al. (1994)	Silicon oil/Ar		1700 ± 110	Emission of excited-state $Cr(CO)_6$ [20]
Misik et al. (1995)	Water/Ar	3000 ± 1000		comparative rate thermometry (isotope effect) [15]
Misik et al. (1996)	Toluene/Ar	6000		comparative rate thermometry (isotope effect) [21]

temperature of water increases with irradiation time. Therefore, the power, P (W), can be calculated by using Eq. (1.2),

$$P = \mathrm{d}T/\mathrm{d}t C_p M \tag{1.2}$$

where $\mathrm{d}T/\mathrm{d}t$ is the temperature rise per second (K s^{-1}), C_p is the heat capacity of water (4.2 J g^{-1}), and M is the mass of water (g). One example is shown in Fig. 1.1, where 500 mL water is irradiated at different ultrasound frequencies of 26, 78, and 130 kHz with nominal ultrasound power of 50 W. The changes in solution temperature during sonication are measured under 150 rpm with a propeller to get a homogeneous value of temperature. From Fig. 1.1, P can be calculated as Table 1.3.

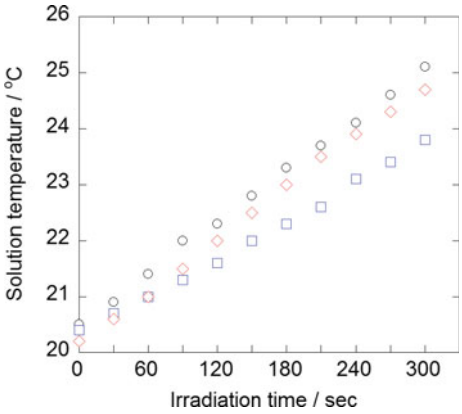

Fig. 1.1 Changes in solution temperature during sonication at different frequencies. (open circle): 26 kHz, (open blue square): 78 kHz, (open red diamond): 130 kHz (Kaijo: Quava mini, nominal power: 50 W)

Table 1.3 Power calorimetrically measured at different ultrasound frequencies with nominal ultrasound power of 50 W

Frequency (kHz)	dT/dt	Power (W)
26	0.0152	31.9
78	0.0113	23.7
130	0.0155	32.6

It should be noted that the calorimetrically measured ultrasound power is lower than the nominal ultrasound power and often different among ultrasound frequencies.

1.3 Chemical Effects of Acoustic Cavitation in Water

When ultrasound is irradiated to water, the pyrolysis of water occurs to form OH radicals and H atoms as

$$H_2O \rightarrow \cdot OH + \cdot H \tag{1.3}$$

The lifetimes of these primary radicals formed are too short to be measured directly by an electron spin resonance (ESR) method. Therefore, these radicals are converted to a long lifetime product using a spin trapping reagent such as 5, 5-dimethyl-1-pyrroline *N*-oxide (DMPO) and 2-methyl-*N*-(4-pyridinylmethylene)-2-propanamine N, N′-dioxide, and then the signals attributed to spin adducts are measured by an ESR method [26]. An example of the reaction of DMPO with OH radical is shown in Eq. (1.4):

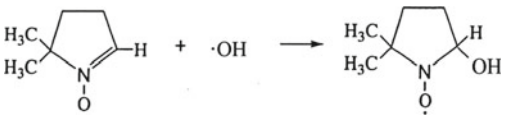

DMPO OH-adduct (1.4)

As another method to confirm the formation of OH radicals, aqueous terephthalate solution is sonicated and the yield of hydroxyl terephthalate formed from the reaction of terephthalate with OH radicals is measured by a fluorescence spectrophotometer [27]. The fluorescence intensity of hydroxyl terephthalate is strong so that the formation of OH radicals can be confirmed with a high sensitivity.

In pure water, the following recombination reactions occur under a noble gas atmosphere:

$$2 \cdot \mathrm{OH} \rightarrow \mathrm{H_2O_2} \tag{1.5}$$

$$2 \cdot \mathrm{H} \rightarrow \mathrm{H_2} \tag{1.6}$$

$$\cdot\mathrm{OH} + \cdot\mathrm{H} \rightarrow \mathrm{H_2O} \tag{1.7}$$

The yields of primary products of H_2O_2 or H_2 are the useful indicators to understand the chemical performance of a used ultrasound apparatus and irradiation system. The Fricke method [28] and KI method [29] can be used to measure the yield of H_2O_2 and/or OH radicals by a UV–vis spectrophotometer.

Figure 1.2 shows the changes in the concentration of Fe(III) formed during sonication of acidic aqueous Fe(II) solution (Fricke solution), where the following reactions proceed during sonication:

$$\mathrm{Fe(II)} + \mathrm{H_2O_2} \rightarrow \mathrm{Fe(III)} + \cdot\mathrm{OH} + \mathrm{OH^-} \tag{1.8}$$

$$\mathrm{Fe(II)} + \cdot\mathrm{OH} \rightarrow \mathrm{Fe(III)} + \mathrm{OH^-} \tag{1.9}$$

Since one mole of H_2O_2 can oxidize two moles of Fe(II) to Fe(III), the following equation is established:

$$[\mathrm{Fe(III)}] = 2[\mathrm{H_2O_2}] \tag{1.10}$$

Therefore, by measuring the concentration of Fe(III) by UV–vis spectroscopy (the mole absorption coefficient of Fe(III) is 2194 M^{-1} cm^{-1} at 304 nm), the yield of H_2O_2 can be measured. Figure 1.2 shows that the yield of Fe(III) increases linearly under Ar and N_2. The yield of Fe(III) under Ar is higher than that under N_2. This is due to that the temperature attained in collapsing bubbles under Ar is higher than that under N_2 as shown in Eq. (1.1). On the other hand, for H_2 formed as reaction (1.6), a gas chromatograph with a thermal conductivity detector is useful for the analysis of H_2 in the gas phase of the irradiated solution.

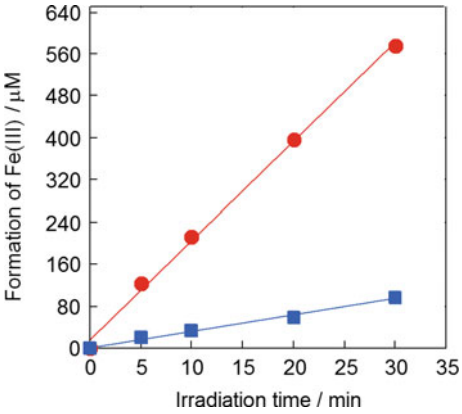

Fig. 1.2 Formation of Fe(III) during sonication of acidic aqueous Fe(II) solution under (red filled circle) Ar and (blue filled square) N_2 (Kaijo: TA-4021; 200 kHz, nominal power: 200 W)

When ultrasound is irradiated to aqueous solution containing an organic compound (RH), OH radicals react with RH so that the degradation of RH proceeds as follows:

$$\mathrm{RH} + \cdot\mathrm{OH} \rightarrow \text{degradation} \tag{1.11}$$

When the degradation of RH [for example, 5, 10, 15, 20-tetrakis (4-sulfotophenyl) porphyrin] occurs mainly by the reaction with OH radicals, the degradation amount of RH could correlate to the yield of OH radicals [30]. The reactivity of OH radicals with RH is also described in Sect. 1.6.

When sonication was performed under an air dissolved solution, the oxidation of N_2 proceeds in collapsing bubbles with high temperatures and pressures. Under a high-temperature condition, N_2 oxidation occurs based on Zeldovich mechanism as shown in Eqs. (1.12–1.17) to form NO_x [31, 32]. It should be noted that the double bond of O_2 (binding energy of O=O: 494 kJ/mol) is more easily broken than the triple bond of N_2 (binding energy of N≡N: 942 kJ/mol).

$$\mathrm{O_2} + \mathrm{M} + 2\mathrm{O} + \mathrm{M} \tag{1.12}$$

$$\mathrm{N_2} + \mathrm{O} \rightarrow \mathrm{NO} + \mathrm{N} \tag{1.13}$$

$$\mathrm{N} + \mathrm{O_2} \rightarrow \mathrm{NO} + \mathrm{O} \tag{1.14}$$

$$2\mathrm{NO} + \mathrm{O_2} \rightarrow 2\mathrm{NO_2} \tag{1.15}$$

$$\mathrm{NO} + \mathrm{NO_2} \rightarrow \mathrm{N_2O_3} \tag{1.16}$$

$$\mathrm{NO} + \mathrm{O} \rightarrow \mathrm{NO_2} \tag{1.17}$$

Since NO and NO_2 react with OH radicals and water, the formation of NO_2^- and NO_3^- occurs [31, 32].

The sonochemical yield [33] or sonochemical efficiency (SE) [34] is sometimes used to explain the chemical performance of the used ultrasound irradiation system. For example, SE can be defined as follows:

$$SE = (Y \times V)/P \tag{1.18}$$

where Y is the yield of a sonochemical reaction (for example, unit: mol L^{-1}), V is the volume (unit: L), and P is the calorimetric power (unit: W). The rate of a sonochemical reaction (unit: mol L^{-1} min^{-1}) can be also used for Y. The yield or the rate of H_2O_2 formed in the sonolysis of pure water is often used for Y in the calculation of SE.

The distribution and density of bubbles which produce OH radicals from the pyrolysis of water can be monitored by light emitted from luminol luminescence because the reaction of luminol with OH radicals occurs to produce an excited state of luminol. Light based on the excited state formed from sonochemical reactions is referred to as "sonochemiluminescence". Examples are shown in Fig. 1.3, where ultrasound irradiation is performed from bottom to top to produce a standing wave and the effect of ultrasound power on the luminol luminescence is investigated under air at 30 °C. It can be seen that the light intensity increased with increasing ultrasound power. Furthermore, a striped pattern can be seen. The width of bright lines corresponds to the half-wavelength of ultrasound, because active bubbles are formed at the antinode of standing wave.

A light scattering method with diode laser beam (for example, 50 mW, 684 nm) is used to analyze the distribution and density of bubbles in solution [35]. In the case of a standing wave irradiation system, the light intensity scattered from antinode is higher than that from node, because a lot of bubbles are formed at antinode. A stroboscope method can be used to analyze the bubble size and motion during acoustic cavitation [36].

1.4 Relationship Between Ultrasound Power and Sonochemical Reaction

Figure 1.4 shows the yield of I_2 as a function of ultrasound power for different solution volumes of 5, 15, 25, and 40 mL [37], where I_2 is formed by the reaction with H_2O_2 and the yield of I_2 (corresponding to I_3^-) can be monitored by UV–vis spectroscopy,

$$H_2O_2 + 2I^- \rightarrow 2OH + I_2 \tag{1.19}$$

$$I_2 + I^- \rightarrow I_3^- \tag{1.20}$$

where the mole absorption coefficient of I_3^- is 26,000 M^{-1} cm^{-1} at 352 nm. From Fig. 1.4, at low ultrasound power, the yield of I_2 increased with increasing ultrasound

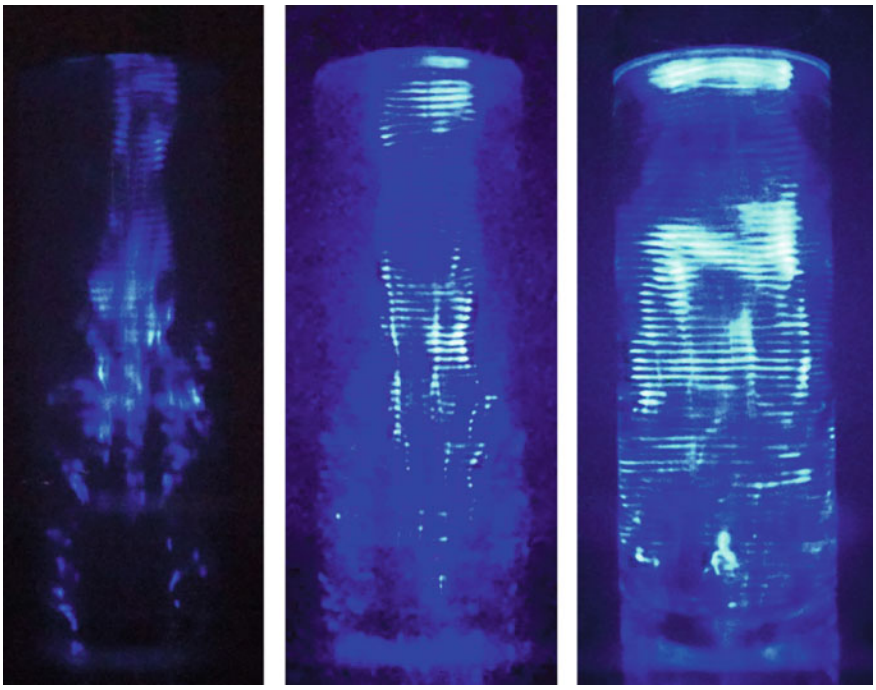

Fig. 1.3 Sonochemiluminescence from aqueous luminol solution under air at 30 °C. From left to right corresponds to power dial of 6, 8, and 10 (Kaijo: TA-4201; 200 kHz, nominal power at power dial 10 is 200 W). Camera: Sony α7s ILCE-7S, exposure time: 2 s. f-number: F2.0, ISO: 64,000

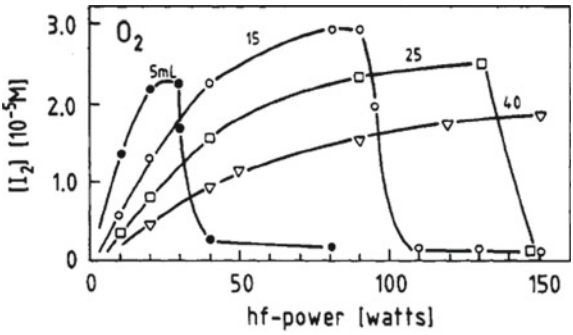

Fig. 1.4 Yield of I_2 as a function of ultrasound power (hf power) for various volumes of the irradiated solution. Condition: 1 MHz, O_2 atmosphere. Reprinted with permission from Ref. [37]. Copyright 1993 American Chemical Society

power. However, at high ultrasound power for 5, 15, and 25 mL solutions, the yield decreased with increasing ultrasound power. When the solution volume is smaller, the drop of the yield occurred at lower ultrasound power. Two reasons for the drop are explained: (1) the size of bubble exceeded the size of active bubble rapidly by one cycle of ultrasound, resulting in the formation of a non-active large bubble, and

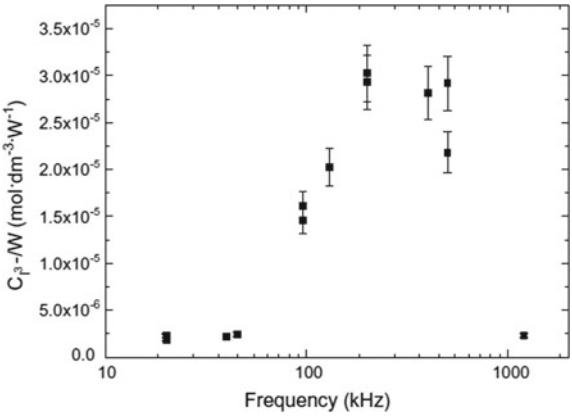

Fig. 1.5 Frequency dependence of chemical effects per unit power. Condition: KI oxidation, 50 mL, air atmosphere, 30 °C. Reprinted with permission from Ref. [34]. Copyright 2003 Elsevier

(2) the formation of larger number of bubbles resulted in the coalescence of bubbles so that the size of bubbles became larger than that of active bubbles.

In addition, it should be noted two points: (1) higher ultrasound power does not always provide higher H_2O_2 formation: the optimum ultrasound power exists for the efficient sonochemical reactions, and (2) H_2O_2 formation is not related linearly to ultrasound power. Accordingly, the sonochemical efficiency shown in Eq. (1.18) should be used for the discussion basically in the linear relationship range between the ultrasound power and the yield of H_2O_2.

1.5 Relationship Between Ultrasound Frequency and Sonochemical Reaction

To investigate the effect of ultrasound frequency is a difficult research subject in sonochemistry. This is because the ultrasound oscillator has an optimum thickness to generate high-intensity ultrasound. This thickness is called as "resonance thickness" and corresponds to the half-wavelength (or which multiplied by integer) of ultrasound generated. Therefore, in general, when the effects of ultrasound frequency are investigated, different ultrasound oscillators and/or generators have been often used.

KI oxidation in 50 mL aqueous solution was investigated by using seven types of sonochemical apparatus in the frequency range of 19.5 kHz–1.2 MHz [34], where $C_{I3}{}^{-}/W$ was measured as the concentration of the formed $I_3{}^{-}$ per unit ultrasound power (calorimetric power). C_{I3}^{-}/W can be considered as a kind of SE, because $C_{I3}{}^{-}/W$ corresponds to SE/V according to Eq. (1.18). It can be seen in Fig. 1.5 that the highest $C_{I3}{}^{-}/W$ existed in the range of 200–500 kHz.

The liquid height of the sample solution also affects the sonochemical efficiency. When the sonochemical efficiency of a cylindrical sonochemical reactor was inves-

tigated as a function of frequency (45, 129, 231, and 490 kHz) and liquid height (10–700 mm), the following equation was proposed [38]:

$$h_{\text{peak}} = (23{,}000/f) - 22.9 \tag{1.21}$$

where h_{peak} is the liquid height (mm) at the peak of the SE value (mol J^{-1}) and f is the ultrasound frequency (kHz). To get a high sonochemical efficiency, the liquid height is one of the important parameters. However, the size, number, size distribution, lifetime of bubbles, and their bubble dynamics are affected by ultrasound frequency as well as power; therefore, the effect of ultrasound frequency is still important research subject to be clarified in sonochemistry.

1.6 Reactions of Organic Additives with OH Radicals in Aqueous Solution

OH radicals have high redox potential (2.85 V) and high reactivity. As a result, they react with most of the organic compounds quickly. As representative reactions, hydrogen abstraction reactions for alkyl chains and electrophilic addition for electron-rich bonds proceed.

The interface of bubbles in aqueous solution is in a high energy state because of high surface tension of water. For such a state, organic molecules in water tend to accumulate at the bubble interface to reduce the surface tension of aqueous solution. Therefore, organic compounds with higher hydrophobicity than that of water tend to accumulate more easily at the interface and surrounding regions of cavitation bubbles [39, 40].

Figure 1.6 shows the rates of H_2O_2 formation during ultrasound irradiation in the absence and presence of alcohols [41]. The rates of H_2O_2 formation decrease with increasing alcohol concentration. This is because alcohols act as OH radical scavengers. The order of the OH radical scavenging effect is 1-butanol > 1-propanol > ethanol at the same alcohol concentration and this order is in the order of hydrophobicity. In general, hydrophobicity of an organic compound can be defined by log P, where P is the octanol–water partition coefficient and P is determined by the following equation:

$$P = C_{\text{octanol}}/C_{\text{water}} \tag{1.22}$$

where C_{octanol} and C_{water} are the concentrations of an organic compound in octanol and water, respectively. A compound with a higher log P value corresponds to a higher hydrophobic one. The log P values for 1-butanol, 1-propanol, and ethanol are 0.839, 0.329, and −0.18, respectively.

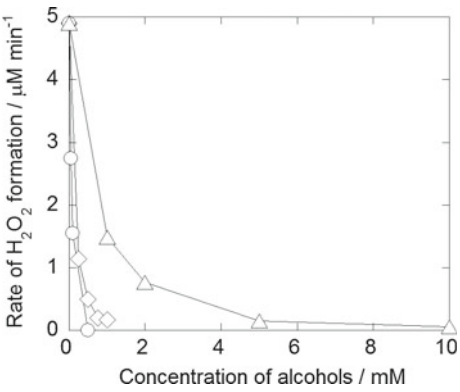

Fig. 1.6 Rates of H_2O_2 formation in the sonolysis of Ar-saturated water in the presence of various concentrations of alcohols. (open circle): 1-butanol, (open diamond): 1-propanol, and (open triangle): ethanol. Reprinted with permission from Ref [41]. Copyright 2016 Elsevier

For the accumulation of an organic compound to the interface of bubbles, Gibbs surface excess (Γ) of the organic compound is a useful indicator to discuss the reaction occurring at the interface of bubbles. Γ can be calculated using the following equation:

$$\Gamma = (-1/kT)(\mathrm{d}\gamma/\mathrm{d}\ln C) \tag{1.23}$$

where γ is the surface tension of the solution and C is the bulk concentration of organic compound. See literature [42–48] to understand the accumulation and behavior of organic compounds at the interface region of bubbles in water.

1.7 Chemical Effects of Acoustic Cavitation in Organic Solvents

When an organic solvent is sonicated, the solvent is pyrolyzed to form various radicals and products. For example, when decane ($C_{10}H_{22}$) was sonicated, H_2, and hydrocarbons such as CH_4, C_2H_6, C_2H_4, C_2H_2, C_3H_8, C_3H_6, etc. are formed [49–51]. The representative reactions of decane under a noble gas are shown in the following equations:

$$C_{10}H_{22} \rightarrow \cdot R_1 + \cdot R_2 + \cdot R_3 + (\cdots) + \cdot R_9 \tag{1.24}$$

$$\cdot R_{2n} \rightarrow C_2H_4,\ \cdot H,\ \cdot C_2H_5 \tag{1.25}$$

$$\cdot R_{2n+1} \rightarrow C_2H_4,\ \cdot CH_3 \tag{1.26}$$

$$C_{10}H_{22} + \cdot R \rightarrow \cdot C_{10}H_{21} + RH \tag{1.27}$$

$$\cdot C_{10}H_{21} \rightarrow C_2H_4 + \cdot R \tag{1.28}$$

$$\cdot C_{10}H_{21} \rightarrow \text{1-alkene}, C_2H_4,\ \cdot R \tag{1.29}$$

$$\cdot R + \cdot R \rightarrow R\text{-}R \tag{1.30}$$

$$\cdot R + \cdot H \rightarrow R\text{-}H \tag{1.31}$$

$$\cdot H + \cdot H \rightarrow H\text{-}H \tag{1.32}$$

In these reactions, H_2 and CH_4 are the main products [49–51]. Therefore, the degree of organic solvent sonolysis can be understood by measuring the yields of H_2 and CH_4 formed, which are measured by a gas chromatograph. These formation efficiencies could be considered as the sonochemical efficiency in the sonolysis of organic solvent [50, 51].

1.8 Physical Effects of Acoustic Cavitation

Acoustic cavitation provides mechanical effects as shockwaves and micro-jets. These effects are generally regarded as physical effects of acoustic cavitation and have been practically applied in biology, medicine, and engineering. Here, some characterization methods for physical effects of acoustic cavitation are introduced. As a typical method, a hydrophone of a piezoelectric material is used to confirm whether cavitation occurs or not in the irradiated solution [52, 53]. In general, when cavitation occurs, broadband noise (noise in the wide range of frequency) can be observed.

For a convenient but rough method, the damage of aluminum foil dipped in the irradiation solution is useful. Figure 1.7 shows a photograph of aluminum foil after 2 min irradiation with a standing wave-type sonication system of (a) 26 kHz and (b) 130 kHz. In the case of 26 kHz irradiation, aluminum foil at around center of bottom side has large holes and many pits are observed in Fig. 1.7a. These are due to shockwaves or micro-jets of acoustic cavitation. In general, the size of bubbles during acoustic cavitation increases with decreasing ultrasound frequency used [2]. Large bubble dynamics result in strong shockwaves or micro-jets. Therefore, a low ultrasound frequency is generally used for a conventional ultrasound cleaning bath to obtain efficient cleaning. When one wants to decrease the effects of shockwaves or micro-jet streams of acoustic cavitation, a higher ultrasound frequency can be used to produce small bubble dynamics. An example is shown in Fig. 1.7b. When 130 kHz ultrasound was irradiated, it was difficult to observe the formation of holes and pits.

Physical effects of acoustic cavitation are observed in the sonolysis of solution including microorganism [54, 55], polymer [56, 57], two liquid phases to emulsification [58], or solid powder [59, 60].

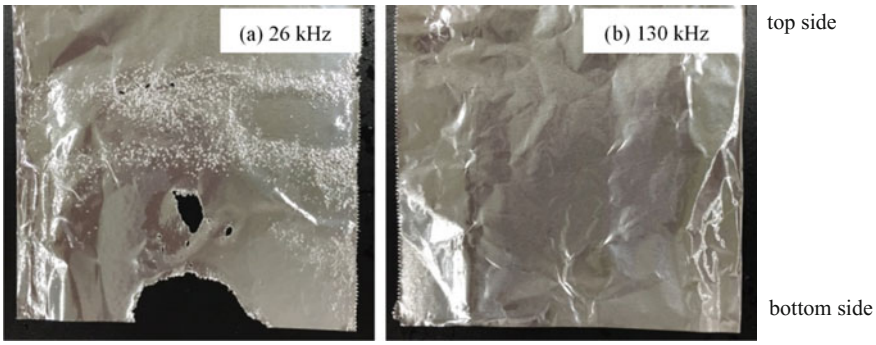

Fig. 1.7 Damage of aluminum foil by acoustic cavitation with a standing wave-type sonication system. **a** 26 kHz, **b** 130 kHz. Bottom side of aluminum foil is located just on oscillator (Kaijo: Quava mini: nominal power is 50 W, irradiation time: 2 min)

References

1. R. Tronson, M. Ashokkumar, F. Grieser, Comparison of the effects of water-soluble solutes on multibubble sonoluminescence generated in aqueous solutions by 20- and 515-kHz pulsed ultrasound. J. Phys. Chem. B **106**, 11064–11068 (2002)
2. K.R. Weninger, C.G. Camara, S.J. Putterman, Observation of bubble dynamics within luminescent cavitation clouds: sonoluminescence at the nano-scale. Phys. Rev. E **63**, 016310 (2001)
3. K. Yasui, T. Tuziuti, J. Lee, T. Kozuka, A. Towata, Y. Iida, The range of ambient radius for an active bubble in sonoluminescence and sonochemical reactions. J. Chem. Phys. **128**, 184705 (2008)
4. K. Yasui, *Acoustic Cavitation and Bubble Dynamics, Ultrasound and Sonochemistry* (Springer Briefs in Molecular Science, Springer, 2018)
5. E.A. Neppiras, Acoustic cavitation. Phys. Rep. **61**, 159–251 (1980)
6. Kagaku-binran, II-233-234. Ed by The Chemical Society of Japan, Maruzen, Japan (1993)
7. C. Sehgal, R.P. Steer, R.G. Sutherland, R.E. Verrall, Sonoluminescence of argon saturated alkali metal salt solutions as a probe of acoustic cavitation. J. Chem. Phys. **70**, 2242–2248 (1979)
8. D. Peters, Ultrasound in materials chemistry. J. Mater. Chem. **6**, 1605–1618 (1996)
9. T. Tuziuti, S. Hatanaka, K. Yasui, T. Kozuka, H. Mitome, Effect of ambient-pressure reduction on multibubble sonochemiluminescence. J. Chem. Phys. **116**, 6221–6227 (2002)
10. K. Okitsu, T. Suzuki, N. Takenaka, H. Bandow, R. Nishimura, Y. Maeda, Acoustic multi-bubble cavitation in water: a new aspect of the effect of rare gas atmosphere on bubble temperature and its relevance to sonochemistry. J. Phys. Chem. B **110**, 20081–20084 (2006)
11. Kagaku-binran, II-234-235. Ed by The Chemical Society of Japan, Maruzen, Japan (1993)
12. Kagaku-binran, II-66. Ed by The Chemical Society of Japan, Maruzen, Japan (1993)
13. Kagaku-binran, II-156-157. Ed by The Chemical Society of Japan, Maruzen, Japan (1993)
14. K.S. Suslick, R.E. Cline, D.A. Hammerton, The Sonochemical Hot Spot. J. Am. Chem. Soc. **108**, 5641–5642 (1986)
15. V. Misik, N. Miyoshi, P. Riesz, EPR spin-trapping study of the sonolysis of H_2O/D_2O mixtures: Probing the temperatures of cavitation regions. J. Phys. Chem. **99**, 3605–3611 (1995)
16. B.E. Nolingk, E.A. Nepprias, Cavitation produced by Ultrasonics. Proc. Phys. Soc. B **63B**, 674–684 (1950)
17. E.J. Hart, A. Henglein, Sonolytic decomposition of nitrous oxide in aqueous solution. J. Phys. Chem. **90**, 5992–5995 (1986)
18. E.J. Hart, C.-H. Fischer, A. Henglein, Sonolysis of hydrocarbons in aqueous solution. Radiat. Phys. Chem. **36**, 511–516 (1990)

19. J.B. Jeffries, R.A. Copeland, E.B. Flint, K.S. Suslick, Thermal equilibration during cavitation. Science **256**, 248 (1992)
20. K.S. Suslick, K.A. Kemper, Pressure measurements during acoustic cavitation by sonoluminescence, in *Bubble Dynamics and Interface Phenomena*, ed. by J.R. Blake (Kluwer, Dordrecht, Netherlands, 1994), pp. 311–320
21. V. Misik, P. Riesz, EPR study of free radicals induced by ultrasound in organic liquids II. Probing the temperatures of cavitation regions. Ultrason. Sonochem. **3**, 25–37 (1996)
22. A. Tauber, G. Mark, H.-P. Schuchmann, C. von Sonntag, Sonolysis of tert-butyl alcohol in aqueous solution. J. Chem. Soc., Perkin Trans. **2**, 1129–1135 (1999)
23. M. Ashokkumar, F. Grieser, A comparison between multibubble sonoluminescence intensity and the temperature within cavitation bubbles. J. Am. Chem. Soc. **127**, 5326–5327 (2005)
24. N.C. Eddingsaas, K.S. Suslick, Evidence for a plasma core during multibubble sonoluminescence in sulfuric acid. J. Am. Chem. Soc. **129**, 3838–3839 (2007)
25. T. Kimura, T. Sakamoto, J.-M. Leveque, H. Sohmiya, M. Fujita, S. Ikeda, T. Ando, Standardization of ultrasonic power for sonochemical reaction. Ultrason. Sonochem. **3**, S157–S161 (1996)
26. K. Makino, M.M. Mossoba, P. Riesz, Chemical effects of ultrasound on aqueous solutions. Formation of hydroxyl radicals and hydrogen atoms. J. Phys. Chem. **87**, 1369 (1983)
27. X. Fang, G. Mark, C. von Sonntag, OH radical formation by ultrasound in aqueous solutions. Part I: The chemistry underlying the terephthalate dosimeter. Ultrason. Sonochem. **3**, 57–63 (1996)
28. A.K. Jana, S.N. Chatterjee, Estimation of hydroxyl free radicals produced by ultrasound in Fricke solution used as a chemical dosimeter. Ultrason. Sonochem. **2**, S87–S91 (1995)
29. E.J. Hart, A. Henglein, Free radical and free atom reactions in the sonolysis of aqueous iodide and formate solutions. J. Phys. Chem. **89**, 4342–4347 (1985)
30. H. Nomura, S. Koda, K. Yasuda, Y. Kojima, Quantification of ultrasonic intensity based on the decomposition reaction of porphyrin. Ultrason. Sonochem. **3**, S153–156 (1996)
31. C.A. Wakeford, R. Blackburn, P.D. Lickiss, Effect of ionic strength on the acoustic generation of nitrite, nitrate and hydrogen peroxide. Ultrason. Sonochem. **6**, 141–148 (1999)
32. V. Misik, P. Riesz, Nitric oxide formation by ultrasound in aqueous solutions. J. Phys. Chem. **100**, 17986–17994 (1996)
33. J. Berlan, T.J. Mason, Sonochemistry: from research laboratories to industrial plants. Ultrasonics **30**, 203–212 (1992)
34. S. Koda, T. Kimura, T. Kondo, H. Mitome, A standard method to calibrate sonochemical efficiency of an individual reaction system. Ultrasonics Sonochem. **10**, 149 (2003)
35. T. Tuziuti, K. Yasui, Y. Iida, Spatial study on a multibubble system for sonochemistry by laser-light scattering. Ultrasonics Sonochem. **12**, 73–77 (2005)
36. T. Kozuka, S. Hatanaka, K. Yasui, H. Mitome, Observation of a Sonoluminescing bubble using a stroboscope. Jpn. J. Appl. Phys. **39**-1-5-B, 2967 (2000)
37. A. Henglein, M. Gutierrez, Sonochemistry and sonoluminescence: effects of external pressure. J. Phys. Chem. **97**, 158–162 (1993)
38. Y. Asakura, T. Nishida, T. Matsuoka, S. Koda, Effects of ultrasonic frequency and liquid height on sonochemical efficiency of large-scale sonochemical reactors. Ultrason. Sonochem. **15**, 244–250 (2008)
39. A. Henglein, C. Kormann, Scavenging of OH radicals produced in the sonolysis of water. Int. J. Radiat. Biol. **48**, 251–258 (1985)
40. M. Ashokkumar, F. Grieser, Single bubble sonoluminescence—a chemist's overview. Chem. Phys. Chem. **5**, 439–448 (2004)
41. K. Okitsu, M. Iwatani, K. Okano, M.H. Uddin, R. Nishimura, Mechanism of sonochemical reduction of permanganate to manganese dioxide in aqueous alcohol solutions: reactivities of reducing species formed by alcohol sonolysis. Ultrason. Sonochem. **31**, 456–462 (2016)
42. A. Henglein, C. Kormann, Scavenging of OH radicals produced in the sonolysis of water. Int. J. Radiat. Biology **48**, 251–258 (1985)

43. A.E. Alegria, Y. Lion, T. Kondo, P. Riesz, Sonolysis of aqueous surfactant solutions: probing the interfacial region of cavitation bubbles by spin trapping. J. Phys. Chem. **93**, 4908–4913 (1989)
44. J.Z. Sostaric, P. Mulvaney, F. Grieser, Sonochemical dissolution of MnO_2 colloids. J. Chem. Soc. Faraday Trans. **91**, 2843–2846 (1995)
45. B. Yim, H. Okuno, Y. Nagata, R. Nishimura, Y. Maeda, Sonolysis of surfactants in aqueous solutions: an accumulation of solute in the interfacial region of the cavitation bubbles. Ultrason. Sonochem. **9**, 209–213 (2002)
46. G.J. Price, M. Ashokkumar, F. Grieser, Sonoluminescence quenching of organic compounds in aqueous solution: frequency effects and implications for sonochemistry. J. Am. Chem. Soc. **126**, 2755–2762 (2004)
47. K. Okitsu, K. Iwasaki, Y. Yobiko, H. Bandow, R. Nishimura, Y. Maeda, Sonochemical degradation of azo dyes in aqueous solution: a new heterogeneous kinetics model taking into account the local concentration of OH radicals and azo dyes. Ultrason. Sonochem. **12**, 255–262 (2005)
48. B. Nanzai, K. Okitsu, N. Takenaka, H. Bandow, Y. Maeda, Sonochemical degradation of various monocyclic aromatic compounds: relation between hydrophobicities of organic compounds and the decomposition rates. Ultrason. Sonochem. **15**, 478–483 (2008)
49. K.S. Suslick, J.J. Gawlenowski, P.F. Schubert, H.H. Wang, Alkane sonochemistry. J. Phys. Chem. **87**, 2299–2301 (1983)
50. K. Okitsu, H. Nakamura, N. Takenaka, H. Bandow, Y. Maeda, Y. Nagata, Sonochemical reactions occurring in organic solvents: reaction kinetics and reaction site of radical trapping with 1,1-Diphenyl-2-Picrylhydrazyl. Res. Chem. Intermediates **30**, 763–774 (2004)
51. Y. Mizukoshi, H. Nakamura, H. Bandow, Y. Maeda, Y. Nagata, Sonolysis of organic liquid: effect of vapour pressure and evaporation rate. Ultrasonics Sonochem. **6**, 203–209 (1999)
52. M. Atobe, T. Nonaka, Ultrasonic effects on electro organic processes. Cavitation threshold values of ultrasound-oscillating power, Chem. Lett. 323–324 (1997)
53. T. Tuziuti, K. Yasui, M. Sivakumar, Y. Iida, N. Miyoshi, Correlation between acoustic cavitation noise and yield enhancement of sonochemical reaction by particle addition. J. Phys. Chem. A **109**, 4869–4872 (2005)
54. Y. Iida, T. Tuziuti, K. Yasui, T. Kozuka, A. Towata, Protein release from yeast cells as an evaluation method of physical effects in ultrasonic field. Ultrason. Sonochem. **15**, 995–1000 (2008)
55. K. Yamamoto, P.M. King, X. Wu, T.J. Mason, E.M. Joyce, Effect of ultrasonic frequency and power on the disruption of algal cells. Ultrason. Sonochem. **24**, 165–171 (2015)
56. G. Portenlanger, H. Heusinger, The influence of frequency on the mechanical and radical effects for the ultrasonic degradation of dextranes. Ultrason. Sonochem. **4**, 127–130 (1997)
57. S. Koda, K. Taguchi, K. Futamura, Effects of frequency and a radical scavenger on ultrasonic degradation of water-soluble polymers. Ultrason. Sonochem. **18**, 276–281 (2011)
58. L.T. Thanh, K. Okitsu, Y. Sadanaga, N. Takenaka, Y. Maeda, H. Bandow, A two-step continuous ultrasound assisted production of biodiesel fuel from waste cooking oils: a practical and economical approach to produce high quality biodiesel fuel. Bioresour. Technol. **101**, 5394–5401 (2010)
59. K.S. Suslick, S.J. Doktycz, The sonochemistry of Zn powder. J. Am. Chem. Soc. **111**, 2342–2344 (1989)
60. H.-M. Hung, M.R. Hoffmann, Kinetics and mechanism of the enhanced reductive degradation of CCl_4 by elemental iron in the presence of ultrasound. Environ. Sci. Technol. **32**, 3011–3016 (1998)

Chapter 2
Synthesis of Metal Nanomaterials with Chemical and Physical Effects of Ultrasound and Acoustic Cavitation

Abstract Six synthesis techniques using ultrasound and acoustic bubbles are introduced. As a technique using chemical effects of acoustic bubbles which comprise high-temperature and high-pressure conditions, (1) a pyrolysis technique (pyrolysis of a volatile metal precursor in organic solvent) and (2) a reduction technique (reduction of metal precursor in water) are described for the synthesis of metal nanoparticles. Furthermore, as a technique using or relating physical effects of ultrasound and acoustic bubbles, (3) ultrasound-assisted, (4) sonomechanical-assisted metal displacement reduction, (5) sonoelectrochemical, and (6) ultrasound spray pyrolysis techniques are introduced. These synthetic techniques will affect the characteristics of the metal nanoparticles and nanomaterials synthesized.

Keywords Pyrolysis · Reduction · Chemical and physical effect · Metal nanoparticle · Metal nanomaterial

2.1 Pyrolysis Technique Using High-Temperature Bubbles

A pyrolysis technique using inside of bubbles is attracted for the synthesis of metal nanoparticles and nanomaterials, because the inside of collapsing bubbles reaches extremely high temperatures and pressures as described in Chap. 1. The pyrolysis technique is generally performed in an organic solvent with a low vapor pressure and metal precursor with an appropriate vapor pressure. For example, when $Fe(CO)_5$ dissolved in decane is irradiated by a horn-type 20 kHz sonicator at 0 °C under noble gas atmosphere, the temperature of collapsing bubbles reaches about 5000 K, where decane is used as a low vapor pressure solvent. Since $Fe(CO)_5$ can enter the inside of collapsing bubbles because of its vaporization, $Fe(CO)_5$ is pyrolized to form Fe atom as shown in Eq. (2.1). The formed Fe atoms aggregate to Fe particles (Eq. 2.2).

$$Fe(CO)_5 \rightarrow Fe + 5CO \tag{2.1}$$

$$nFe \rightarrow Fe_n \tag{2.2}$$

K. Okitsu et al., *Sonochemical Production of Nanomaterials*,
Ultrasound and Sonochemistry, https://doi.org/10.1007/978-3-319-96734-9_2

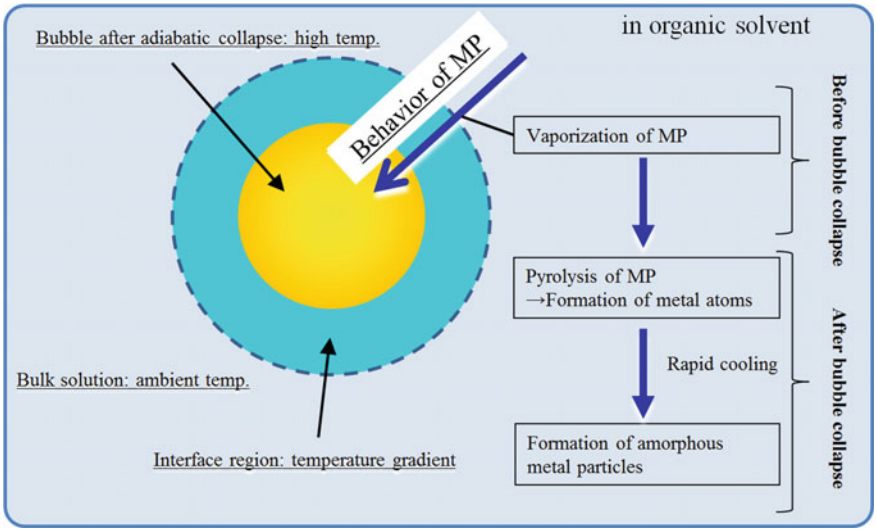

Fig. 2.1 Schematic diagram of the behavior and pyrolysis of metal precursor (MP) and formation of metal nanoparticle in organic solvent. In general, volatile MP is used

A schematic diagram of the synthesis of metal particles in organic solvent is shown in Fig. 2.1.

Extremely high cooling rate (more than 10^{10} K/s) during collapsing bubbles can suppress the formation of crystalline structures of Fe: amorphous Fe particles are formed dominantly [1]. In addition, the size and surface area of the synthesized Fe particles were ~10 nm (TEM analysis) and 120 m^2/g (BET surface area). This surface area was about 120 times larger than that of commercially available Fe powers of 5 μm in diameter. The prepared amorphous Fe particles showed excellent catalytic activities for dehydrogenation and hydrogenolysis of cyclohexane. When a colloidal stabilizer of polyvinylpyrrolidone (PVP) was added in the irradiated 1-octanol solution of $Fe(CO)_5$, the size of amorphous Fe nanoparticles formed became smaller as the diameter range of 3–8 nm [2]. This is because PVP suppresses further growth and aggregation of Fe nanoparticles.

By using the same technique, amorphous Fe nanoparticles on silica (amorphous Fe/SiO_2) can be prepared in the solution including silica particles (Fig. 2.2) [3]. Fe nanoparticles synthesized by this technique are smaller in size and have higher specific surface area than those synthesized by a conventional impregnation method. A higher catalytic activity for the hydrocarbon synthesis from CO and H_2 (the Fischer–Tropsch reaction) was achieved compared with conventional Fe/SiO_2 catalyst [4].

When O_2 gas was used as a dissolved gas instead of noble gas, Fe_2O_3 particles are formed dominantly from the sonolysis of $Fe(CO)_5$ in decalin solution [5]. Therefore, choosing the types of gas is important to control the sonochemical reactions and products of oxidation state. Recently, Enomoto et al. analyzed the products from the

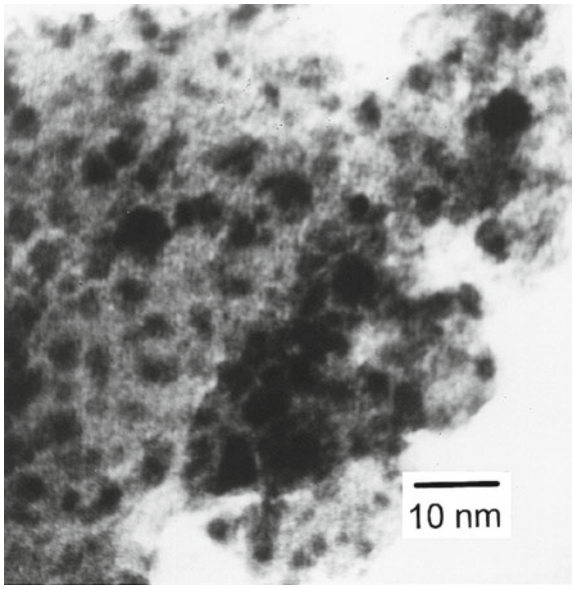

Fig. 2.2 Transmission electron micrograph and electron microdiffraction pattern of nanometer iron particles supported on silica surface, taken on a Phillips EM400T electron microscope. Reprinted with permission from Ref. [3]. Copyright 1996 American Chemical Society

sonolysis of $Fe(CO)_5$ under Ar and pointed out that the amorphous nanoparticles formed are mixture of Fe metal and volatile organic of ~14 wt% [6]. In addition, they insisted that Fe nanoparticles formed are very air-sensitive.

Alloy and bimetallic nanoparticles are also attracted as excellent catalysts, because new function and synergy effects are expected to be emerged. When the decane solution including two volatile precursors of $Fe(CO)_5$ and $Co(CO)_3(NO)$ was irradiated under Ar, Fe–Co alloy nanoparticles can be synthesized. The metal ratio of alloy can be controlled by changing the ratio of these metal precursors. The catalytic activity and selectively of $Fe_{52}Co_{48}$ nanoparticles for dehydrogenation of cyclohexane to benzene at 300 °C was higher than other nanoparticles with different alloy ratios [3].

To achieve a higher yield of nanoparticles and nanomaterials in this technique, it should be noted the following points: (1) use of dissolved gas with higher γ value to produce higher temperature bubbles, (2) use of lower vapor pressure solvent to suppress the decrease in bubble temperature because solvent vapor has low γ value, (3) use of a metal precursor with appropriate vapor pressure to proceed gas phase reactions in bubbles, and (4) use of oxygen gas as a dissolved gas to proceed oxidation of products.

2.2 Reduction Technique Using Sonochemically Formed Reductants

A sonochemical reduction technique can be used for the synthesis of metal nanoparticles in aqueous solution. For example, when aqueous solution includes Au(III), a water-soluble metal precursor such as $AuCl_4^-$ and organic solute (RH) such as an alcohol are sonicated under noble gas atmosphere, various kinds of reducing species (·H, ·R, organic radicals) are formed via radical reactions (Eq. 2.4) and pyrolysis reactions of RH (Eq. 2.5) [7–11],

$$H_2O \rightarrow \cdot OH + \cdot H \tag{2.3}$$

$$RH + \cdot OH(\cdot H) \rightarrow \cdot R + H_2O(H_2) \tag{2.4}$$

$$RH \rightarrow \text{organic radicals} \tag{2.5}$$

where ·R is the radical formed by the abstraction reaction of ·OH (or, ·H) with RH. The formed radicals can reduce Au(III) to Au(II), Au(II) to Au(I), and Au(I) to Au. The disproportionation reaction of Au(II) also proceeds as shown in Eq. (2.9). Finally, Au nanoparticles are formed.

$$\text{Au(III)} + \text{reducing radical} \rightarrow \text{Au(II)} \tag{2.6}$$

$$\text{Au(II)} + \text{reducing radical} \rightarrow \text{Au(I)} \tag{2.7}$$

$$\text{Au(I)} + \text{reducing radical} \rightarrow \text{Au} \tag{2.8}$$

$$2\text{Au(II)} \rightarrow \text{Au(III)} + \text{Au(I)} \tag{2.9}$$

$$n\text{Au} \rightarrow\rightarrow \text{Au}_n \tag{2.10}$$

$$\text{Au}_n + \text{Au} \rightarrow \text{Au}_{n+1} \tag{2.11}$$

A schematic diagram of the synthesis of metal nanoparticle in aqueous solution including RH is shown in Fig. 2.3.

When organic colloidal stabilizers such as PVP, sodium dodecyl sulfate (SDS), polyethylene glycol (PEG), etc. are added in metal nanoparticles synthesis [12, 13], these stabilizers act as a precursor of reductants as in Eqs. (2.4) and (2.5).

By using a sonochemical reduction technique for water-soluble metal ion or complex precursors (e.g., Ag^+, $[PdCl_4]^{2-}$, $[PtCl_4]^{2-}$, $[PtCl_6]^{2-}$, $[AuCl_4]^-$, and MnO_4^-), the corresponding metal nanoparticles of Ag, Pd, Pt, Au, and MnO_2 can be synthesized [7–23]. The formation of these metal nanoparticles is confirmed generally by its UV–vis spectrum, light scattering, XRD, EXAFS, SEM, and TEM.

In a sonochemical reduction technique, the types of dissolved gas, organic additive, and colloidal stabilizer as well as ultrasound power and frequency, solution temperature, and irradiation procedures are effective parameters to control the rate of metal ion reduction [8, 10, 11, 14]. This is because these parameters affect the characteristics of acoustic bubbles. As described in Chap. 1, a dissolved gas in water

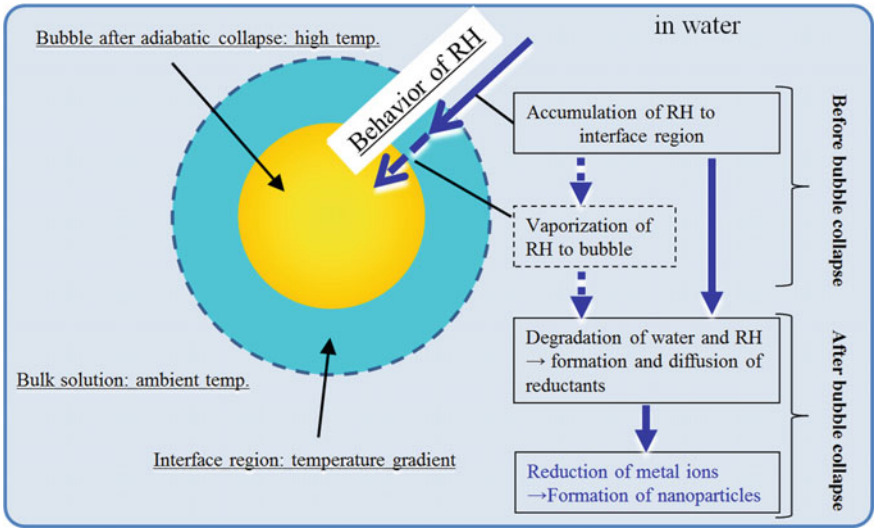

Fig. 2.3 Schematic diagram of the behavior of organic solute (RH) and reduction of metal ions, formation of metal nanoparticle in water. In general, water-soluble RH is used

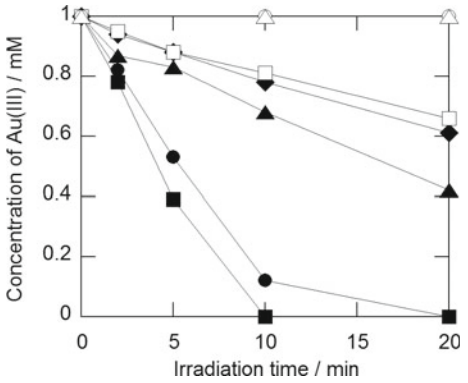

Fig. 2.4 Changes in the concentration of Au(III) during ultrasonic irradiation under various atmospheres. Condition: Intensity; 1.43 W cm^{-2}, 1-propanol; 20 mM, temperature; 20 °C, distance; 4.0 mm. (Filled black square) Kr, (filled black circle) Ar, (filled black up-pointing triangle) Ne, (filled black diamond) He, (open white square) N_2, (open white circle) CO_2, (open white up-pointing triangle) CH_4. Reprinted with permission from Ref. [10]. Copyright 2002 The Chemical Society of Japan

affects the temperature and number of collapsing bubbles. For example, the rate of Au(III) reduction is in the order of CH_4 (no reduction) = CO_2 (no reduction) $\ll N_2$ < He < Ne < Ar < Kr (Fig. 2.4) [10].

Organic solutes in water are tended to accumulate at the interface region of bubbles because they induce a decrease in the surface energy of bubbles [7–11,

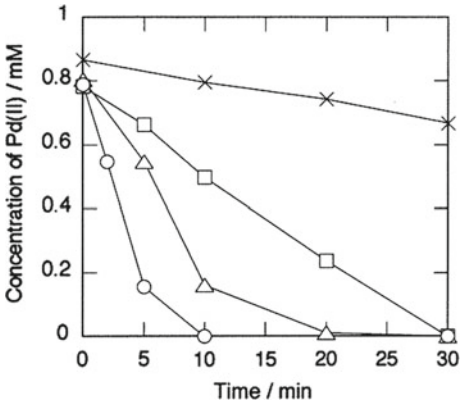

Fig. 2.5 Effect of the type of alcohol on the reduction of Pd(II) under Ar. Condition: 2.02 g/L Al_2O_3, 20 mM alcohol. (X); no alcohol, (open white square); methanol, (open white up-pointing triangle); ethanol, (open white circle); 1-propanol. Reprinted with permission from Ref. [20]. Copyright 2000 American Chemical Society

14, 20]. Because of the extreme high temperature attained in collapsed bubbles, pyrolysis and radical reactions of organic solutes occur to form reducing radicals as in Eqs. (2.4) and (2.5). Figure 2.5 shows changes in the concentration of Pd(II) during sonochemical reduction of Pd(II) in the presence of alumina and 20 mM alcohol [20] under Ar. It can be seen that the rate of Pd(II) reduction is in the order of methanol < ethanol < propanol, although the same concentration of alcohol is included for all experiments. This is because a higher hydrophobic alcohol tends to accumulate at the interface region of bubbles so that a larger amount of reducing radicals are formed. The size of the formed Pd nanoparticles on alumina was in the order of propanol < ethanol < methanol. The size was suggested to be related to the nucleation rate of Pd nanoparticles.

In the absence of organic stabilizer, the size of the formed metal nanoparticles tends to decrease with increasing rate of metal ion reduction [10, 14]. As one example, the relationship between the size of the formed Au nanoparticles and the rate of Au(III) reduction is shown in Fig. 2.6, where a different ultrasound frequency is chosen as an experimental parameter, but calorimetric power among them is controlled as the same power [14]. A clear tendency can be seen in Fig. 2.6, although cavitation phenomena should be different among each ultrasound frequency.

Bimetallic Au/Pd nanoparticles can be synthesized when the sonochemical reduction of Au(III) and Pd(II) was performed simultaneously in aqueous SDS solution under Ar [21]. In this case, the reduction of both of Au(III) and Pd(II) should proceed, because reducing radicals formed from the sonolysis of SDS can reduce both of Au(III) and Pd(II). However, the experimental results which were analyzed by the UV–vis spectra of the irradiated solution indicated that the reduction of Au(III) started at first and then the reduction of Pd(II) started after completion of the reduction of Au(III). The TEM image of the product indicated that the average size of the formed Au/Pd nanoparticles is ca. 8 nm and they have Au core and Pd shell nanostructure. The formation of this core–shell structure is due to the following reaction occurred because of the different redox potentials between $AuCl_4^-$/Au, 1.002 V and $PdCl_4^{2-}$/Pd, 0.620 V:

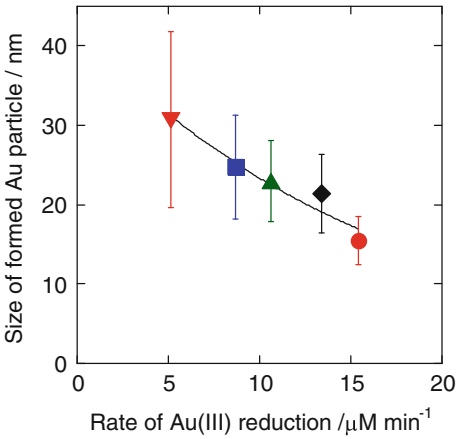

Fig. 2.6 Relationship between size of formed Au nanoparticles and rate of Au(III) reduction under Ar with different ultrasound frequencies. (Filled red down-pointing triangle); 20 kHz, (filled red circle); 213 kHz, (filled black diamond); 358 kHz, (filled green up-pointing triangle); 647 kHz, (filled blue square); 1062 kHz. Au(III): 0.2 mM, 1-propanol: 20 mM, ultrasound intensity: 0.1 W mL^{-1}, irradiation time: 120 min. Reprinted with permission from Ref [14]. Copyright 2005 American Chemical Society

$$3Pd(0) + 2Au(III) \rightarrow 3Pd(II) + 2Au(0) \tag{2.12}$$

That is, the sonochemically formed Pd(0) is oxidized by Au(III) so that Au(III) reduction occurs first.

When the sonochemical reduction of Au(I) formed by mixing Au(III) and ascorbic acid was performed in the presence of cetyltrimethylammonium bromide (CTAB) and $AgNO_3$ under Ar, Au nanorods can be synthesized [24, 25], where CTAB and $AgNO_3$ act as effective capping agents for the growth of Au seeds to Au nanorods. By changing pH of solution or irradiation time, the aspect ratio (ratio of length to width) of nanorods can be controlled. Figure 2.7 shows TEM images of Au nanorods grown via Au seeds formed after (a) 0.5, (b) 1, (c) 3, (d) 10, or (e) 15 min of ultrasound irradiation [25]. It can be seen that the length and width of the resulting Au nanorods decreased with increasing irradiation time. The reason why Au nanorods become larger for shorter irradiation times is because the amount of sonochemically formed Au seeds is smaller for shorter irradiation time, so that the amount of the remaining Au(III) is larger for shorter irradiation time. As a result, the larger amount of Au(III) is distributed to a smaller number of seeds and thus each seed grows largely.

The formation mechanism of Au nanorods is proposed as follows: relatively small Au seeds are formed at short irradiation times, but they rapidly grow to a critical size and thus the size and aspect ratio of the formed Au nanorods depend on the number of Au seeds attaining the critical size [25]. The optical properties of the gold nanorods grown are also controlled by changing their aspect ratio. This should

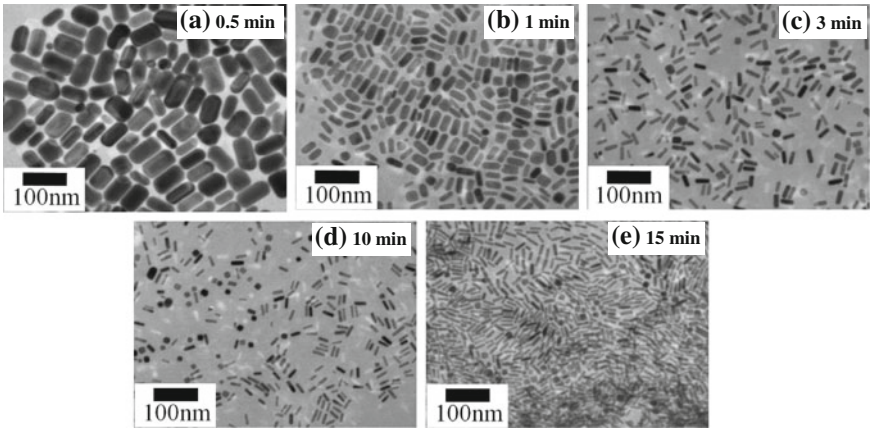

Fig. 2.7 TEM images of Au nanorods produced via Au seeds formed after **a** 0.5, **b** 1, **c** 3, **d** 10, or **e** 15 min of ultrasonic irradiation. Reprinted with permission from [25]. Copyright 2014 Elsevier

be important for their wide variety of applications such as surface-enhanced Raman spectroscopy, imaging, photothermal therapy of cancer cells, and optical recording materials [26, 27].

Manganese oxides can be used as electrochemical capacitors, catalysts, sensors, and adsorbents. The size, shape, and crystal structures of MnO_2 strongly influence their physicochemical properties. MnO_2 can be synthesized by the sonochemical reduction of MnO_4^- under Ar at 20 °C. The solution pH is an effective parameter to control the reduction of MnO_4^- and formation of MnO_2. Poor crystallinity δ-MnO_2 was formed at pH 2.2, 6.0, and 9.3. Figure 2.8 shows SEM and TEM images of the sonochemically synthesized MnO_2 at different pH solutions [22]. When the solution pH was increased from 2.2 to 9.3, the morphologies of δ-MnO_2 changed from aggregated sheet-like or needle-like structures to spherical nanoparticles and finally to cubic or polyhedron nanoparticles. After further irradiation, MnO_2 was readily reduced to Mn^{2+}. It was confirmed that H_2O_2 and H atoms formed in the sonolysis of water acted as reductants for both the reduction for MnO_4^- to MnO_2 and MnO_2 to Mn^{2+}. Taking into account the colloidal stability and size of the formed MnO_2 nanoparticles, pH 6.0 was considered to be the appropriate pH condition for the synthesis of MnO_2 nanoparticles in the reported irradiation system.

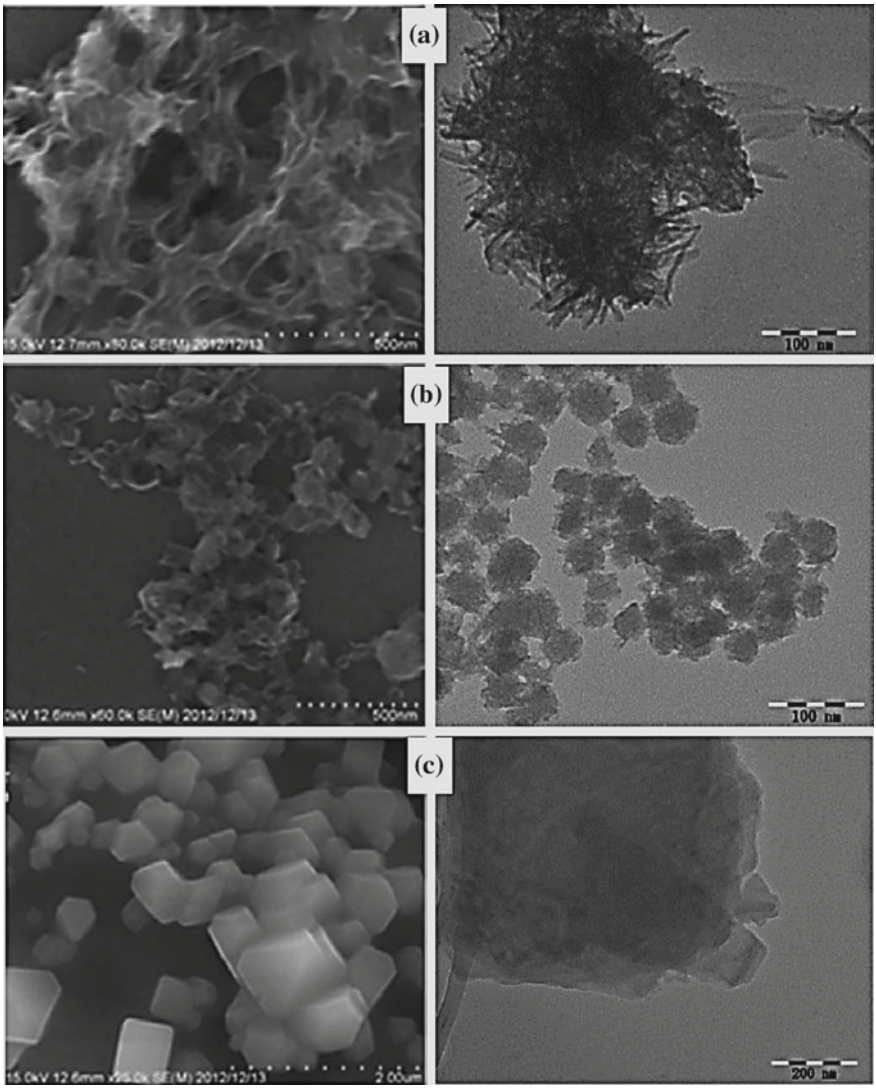

Fig. 2.8 SEM (left) and TEM (right) images of sonochemically synthesized MnO_2 at **a** pH 2.2, **b** pH 6.0, and **c** pH 9.3. Reprinted with permission from [22]. Copyright 2014 Elsevier

2.3 Ultrasound-Assisted Technique

An ultrasound-assisted technique is generally based on physical effects such as shockwaves, micro-jets, micro-stirring, shear forces, and ultrasound vibration. Therefore, this technique can be applied to most of the reactions or material processing including nucleation and/or growth. For examples, MnO_2 nanoparticles can be synthesized by mixing of MnO_4^- and Mn^{2+} as follows [28]:

$$MnO_4^- + Mn^{2+} \rightarrow 2MnO_2 \tag{2.13}$$

This reaction proceeds even in the absence of ultrasound, but the rate of the reaction will be enhanced by acoustic bubbles. MnO_2 synthesized by ultrasound-assisted reactions at pH 3.7 had spherical and flower-like morphologies by analyzing SEM and TEM, respectively. When MnO_2 was synthesized at pH 8.8, MnO_2 nanowires were formed: the morphologies changed by changing pH of the sample solution.

Graphene (rGO), a two-dimensional carbon material with large specific surface area, has outstanding characteristics for electro-conductivity, thermal-conductivity, and mechanical strength and thus rGO has much attention for application in various fields of technologies [29]. Several approaches such as mechanical exfoliation of graphite, chemical vapor deposition of rGO, and chemical reduction of graphene oxide (GO) to rGO in solution have been developed. In solution-based chemical reduction, ultrasound-assisted reduction of GO is effective. For example, Abulizi et al. reported that rGO can be synthesized by ultrasound-assisted reaction of GO, where nontoxic and moderate reductant of L-ascorbic acid (L-AA) was added in a reaction system [30].

Figure 2.9 shows the absorption spectra of the GO dispersions before and after treatment of ultrasound and stir mixing (corresponding to without ultrasound), where the sample solution was analyzed after centrifugation at 13,000 rpm for 10 min to remove L-AA, because L-AA has strong absorption at less than 350 nm. GO and rGO have a typical peak at around 230 nm and 270 nm in the spectrum, respectively [31, 32]. Figure 2.9 also indicated that the absorption peak at 230 nm redshifted to around 270 nm only after ultrasound treatment so that GO was reduced to rGO. This spectrum change is due to that the electronic conjugation is restored [32]. The color of the GO dispersion changed from light brown to black only for ultrasound treatment (Inset Fig. 2.9a). This color change is also information that GO is reduced to rGO. In addition, the absorption in the whole spectral region increases with increasing irradiation time, indicating that GO is reduced to rGO with irradiation time. The reduction of GO to rGO was also confirmed by the results of FT-IR and XRD analyses.

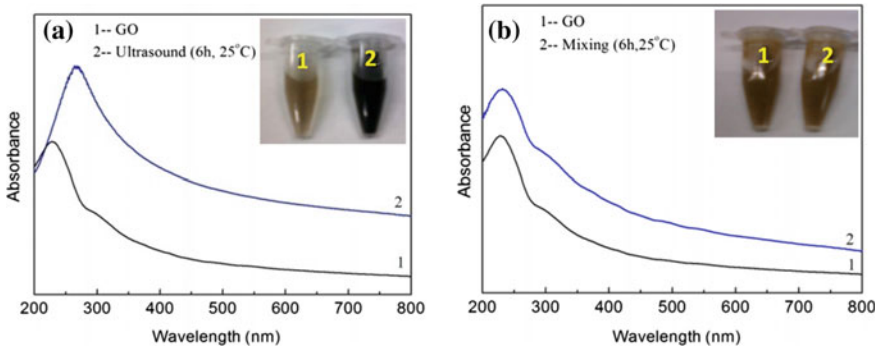

Fig. 2.9 Absorption spectra of GO dispersion and sample solution formed under ultrasound treatment (A) and mixing treatment (B) in the presence of 0.2 g L-AA at pH 11. Insets are the photographs of aqueous dispersions (0.1 mg/mL) of GO before (1) and after (2) ultrasound and mixing treatment at 25 °C for 6 h. Condition of ultrasound treatment: ultrasound power 50%, pulse mode 0.5 s on/0.5 s off. The spectrum 2 in (B) was translated to the upper side to compare the position of the peak wavelength easily. Reprinted with permission from [30]. Copyright 2014 Elsevier

The pseudo-activation energy (E_a) for the reduction of GO to rGO under ultrasound irradiation was about 1.3 times lower than that under the conventional stir mixing without ultrasound [30]. This result was considered that physical effects of acoustic bubbles enhanced the mass transfer of L-AA and GO, and changed the size and the surface morphology of GO. Furthermore, since the rate of GO to rGO was affected by the solution temperature, local high temperatures formed at the interface of cavitation bubbles may also affect the acceleration of the reduction of GO. Since the data in the kinetics were obtained taking into account some assumptions, further investigations are needed to clarify the kinetics.

Ultrasound-assisted exfoliation can be used for the preparation of carbon nanosheets. Carbon nanoscrolls can be prepared from exfoliated graphite sheets by using a high-intensity horn-type sonicator (500 W) [33], where exfoliated graphite sheets are formed from graphite by intercalation of K and ethanol. The degree of scrolling increased from <10% to over 80% by sonication. Khan et al. found that the formation rate of graphene from graphite powders by *N*-methyl-pyrrolidone solvent exfoliation can be enhanced by even low-power ultrasound irradiation with a bath sonicator [34]. When a high-power bath sonicator was used for this experiment, the steady-state temperature of solution increased by more than 50 °C and this temperature increase resulted in the solvent degradation. In sodium cholate aqueous solution, graphene flakes can also be prepared from graphite powders [35].

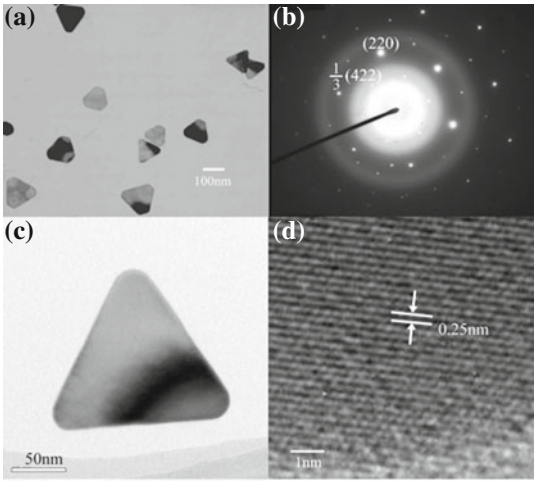

Fig. 2.10 TEM, SAED, and HRTEM images of silver nanoplates: **a** TEM image of as-prepared silver nanoplates, **b** SAED image of silver nanoplates, **c** TEM image of a single crystal, **d** HRTEM image of silver nanoplates. Reprinted with permission from Ref. [36]. Copyright (2004) American Chemical Society

The nucleation and growth of particles are often affected by ultrasound, and thus various types of inorganic and metal nanoparticles can be prepared. Shape-controlled Au and Ag nanoparticles [36] can be synthesized in the presence of *N*,*N*-dimethylformamide (DMF) and PVP, where DMF was used as a solvent and reducing agent. Figure 2.10 shows TEM, selected area electron diffraction (SAED), and HRTEM images of silver nanoplates prepared.

By using both of physical and chemical effects of acoustic cavitation with a high-intensity horn-type sonicator (20 kHz, 50 W/cm^2, 0 °C, Ar), polystyrene functionalized graphene can be prepared from natural graphite flakes in the presence of styrene as a reactive solvent [37]. In this case, radical polymerization of styrene is initiated by the chemical effects of acoustic cavitation.

2.4 Sonomechanical-Assisted Metal Displacement Reduction Technique

A suitable pairing of a metal precursor and metal foil can produce metal nanoparticles under ultrasound irradiation. This technique is called as a sonomechanical-assisted metal displacement reduction technique [38, 39]. For example, when an aqueous 0.0025 M $HAuCl_4$ solution in the presence of 0.05 M PVP (average molecular weight: 58,000) and Cu foil was sonicated by an ultrasound cleaner (42 kHz, 70 W), the changes in UV–vis absorption spectra of the sample solution were observed as shown in Fig. 2.11a. For comparison, Fig. 2.11b shows the results without Cu foil. From

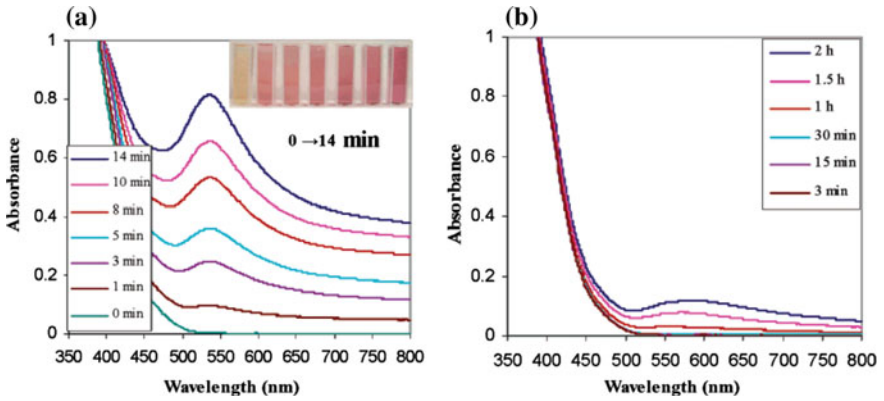

Fig. 2.11 UV–vis absorption spectra of Au colloids sampled at different reaction stages by reducing 0.0025 M $HAuCl_4$ aqueous solutions in 42 kHz continuous ultrasound cleaner at room temperature and in ambient conditions: **a** in the presence of Cu foil as a heterogeneous reducing medium; **b** in the absence of Cu foil (solely ultrasonication). Reprinted with permission from [38]. Copyright 2006 American Chemical Society

Fig. 2.11, it was clear that the absorption intensity of the surface plasmon of Au nanoparticles located at around 530 nm increased with increasing irradiation time in the presence of Cu foil. From TEM observation, Au nanoparticles with 10 nm average diameter were formed by 5 min sonication.

The following metal displacement reaction proceeds:

$$2[AuCl_4]^- + 3Cu\ (foil) \rightarrow 2Au(0) + 3Cu(II) + 8Cl^- \tag{2.14}$$

where $E_{[AuCl_4]^-/Au(0)}$ is 0.93 V and $E_{Cu(II)/Cu(0)}$ is 0.34 V [38]. It is suggested that the formed metal atoms on the metal foil are removed by mechanical effects of acoustic cavitation. When H_2PtCl_6 ($E_{[PtCl_6]^{2-}/Pt(0}$: 0.7 V) and Fe foil ($E_{Fe(II)/Fe(0)}$: −0.44 V) was used as a precursor and foil, Pt nanoparticles with 6 nm average diameter were formed by 5 min sonication [38].

The starting material combination of a metal ion precursor and metal foil is important to produce metal nanoparticles. Nanoparticles of Ag (average size: 51.7 nm), Cu (7.8 nm), Fe_2O_3 (14.4 nm), CoO_x(124 nm), RuO_2 (3.1 nm), and Sn (7.9 nm) were formed from the combination of $AgNO_3$/Co foil, $CuCl_2$/Al foil, $FeCl_2$/Mg foil, $CoCl_2$/Mg foil, $RuCl_3$/Mg foil, and $SnCl_2$/Mg foil [39].

2.5 Sonoelectrochemical Technique

A sonoelectrochemical technique, combined use of an electrochemical technique with ultrasound, is a promising one for nanomaterial synthesis, because physical

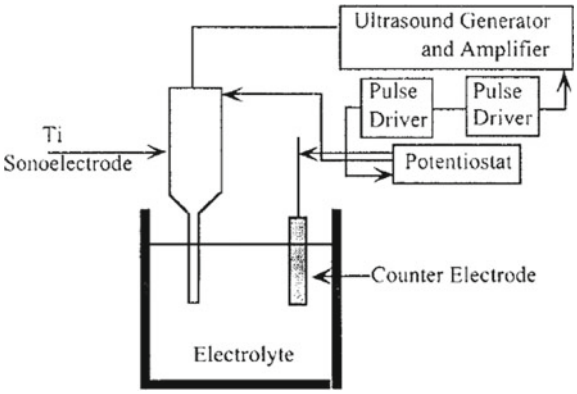

Fig. 2.12 Experimental setup of sonoelectrochemical reaction system. Reprinted with permission from [40]. Copyright 2000 American Chemical Society

effects of acoustic cavitation overcome the demerit of electrochemical processes and improve chemical processes. In general, acoustic cavitation in an electrochemical technique is effective for mixing of solution and thus results in the enhancement of mass transfer of solutes and reduces the thickness of the electric double layer. In addition, cleaning and activation (removal of an undesirable material) of the electrode surface by acoustic cavitation enhance the rate of electrochemical reactions and may change the types and amounts of intermediates, which results in new reaction pathways. Due to these merits, a sonoelectrochemical technique can be used for nanoparticle synthesis.

An example of experimental setup is shown in Fig. 2.12 [40]. A horn-type Ti is used as a sonoelectrode, and Pt sheet is used as a counter electrode. For the preparation of Pd nanoparticles, aqueous solution including H_2PdCl_4 (Pd(II)), KNO_3, NaOH, and a colloidal stabilizer such as CTAB, PVP, and PDDA (polydiallyldimethylammonium chloride) is prepared and chemical reactions are performed with a sonic pulse and a current pulse. This technique corresponds to a pulse sonoelectrochemical technique. When a current density of 25 mA cm^{-2} and an ultrasound intensity of ca. 20 W were applied for 1.5 h, different sizes and shapes of Pd nanoparticles were formed: spherical nanoparticles with ca. 7 nm diameter, multi-twinned nanoparticles with ca. 40 nm, and spherical spongelike nanoparticles with ca. 100 nm were formed in CTAB (pH 8), PVP (pH 6), and PDDA solution (pH 6), respectively [41].

The mechanism of the formation of spherical spongelike nanoparticles is proposed as shown in Fig. 2.13. Pd(II) in solution is electrochemically reduced on the surface of sonoelectrode. Finally, the formed primary Pd nanoparticles are dispersed by physical effects of acoustic cavitation and then their grow, aggregation, and/or Ostwald ripening of particles occur simultaneously. It should be noted that this technique does not need any chemical reductants for metal ion precursors. The following parameters will affect the sonoelectrochemical reactions: type and concentration of a colloidal stabilizer which acts as a size- and/or shape-controlled agent, current

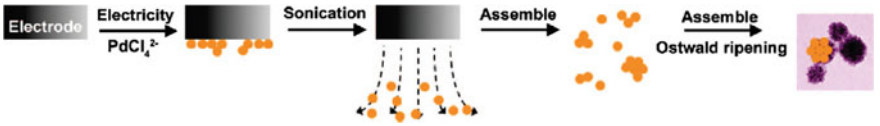

Fig. 2.13 Schematic illustration of the formation of spherical spongelike particles. Reprinted with permission from [41]. Copyright 2009 American Chemical Society

density, reaction time, temperature, ultrasound power, ultrasound frequency, pulse mode, etc.

By using the sonoelectrochemical technique, bimetallic nanoparticles of AuAg [42], CdTe [43], and Au nanoparticle–carbon nanosheet hybrids [44] can be synthesized. In addition, the sonoelectrochemical technique can be used for anodization of Ti foil to synthesize TiO_2 nanotubular arrays [45], where the pore diameter and nanotube length are tuned by changing the applied potential and anodization time.

2.6 Ultrasound Spray Pyrolysis Technique

When ultrasound is irradiated from bottom to upper side in a liquid, depending on the irradiation condition, mists (liquid droplets) are generated. The size of liquid droplets formed by ultrasound has a narrow size distribution compared with that formed by a conventional spray method. The average size (d_{av}) of the droplets is reported to be as follows:

$$d_{av} = 0.34(8\pi\gamma/\rho f^2)^{1/3} \tag{2.15}$$

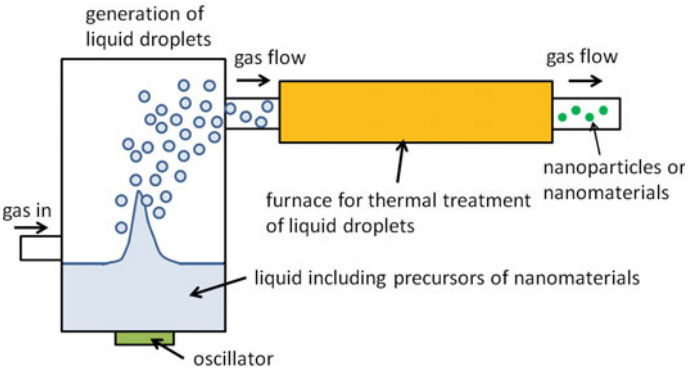

Fig. 2.14 Image of ultrasound spray pyrolysis

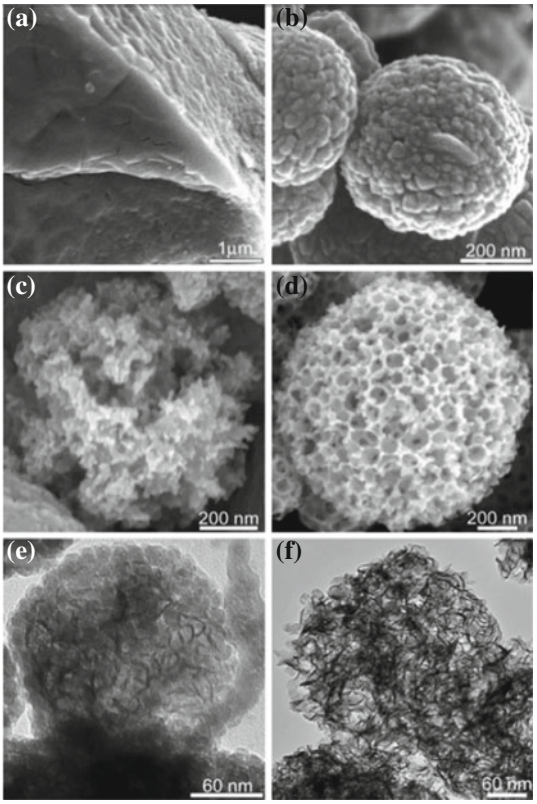

Fig. 2.15 Electron micrographs of conventional and ultrasonic spray pyrolysis (USP)-derived MoS_2. **a** SEM of conventional MoS_2. **b** SEM of USP MoS_2 without templating material. **c** SEM of 20 nm silica-templated USP MoS_2, after leaching of the colloidal silica. **d** SEM of 80 nm silica-templated USP MoS_2, after leaching of the colloidal silica. **e** TEM of USP SiO_2/MoS_2 composite (prior to leaching, 20 nm SiO_2 template). **f** TEM of 20 nm silica-templated USP MoS_2, after leaching of the colloidal silica. Reprinted with permission from [50]. Copyright 2005 American Chemical Society

where γ is the surface tension of the liquid (mN/m), ρ is the liquid density (g/cm^3), and f is the ultrasound frequency (Hz) [46]. This equation indicates that d_{av} of the droplets decreases with increasing ultrasound frequency. By using Eq. (2.15), d_{av} of the droplets formed from 2.0 MHz ultrasound irradiation to pure water and ethanol can be calculated to be 2.8 μm and 1.9 μm, respectively.

Figure 2.14 shows an example of experimental setup for the formation of liquid droplets including precursors by ultrasound irradiation and the thermal treatment of these liquid droplets. This technique is called as ultrasound spray pyrolysis one. By using this technique, various ceramic nanomaterials [47, 48] of Y_2O_3–ZrO_2, $BaTiO_3$–$SrTiO_3$, ZnS, Y_2O_3:Eu^{3+}, and NiO, and semiconductor nanoparticles [49] of CdS, CdSe, and CdTe can be prepared. Recently, porous nanostructures can be

prepared with inorganic or organic templates. For example, porous MoS_2 particles can be prepared by aqueous solution including $(NH_4)_2MoS_4$ and colloidal silica as a sacrificial template which can be removed by HF treatment after thermal treatment of liquid droplets [50]. The prepared MoS_2 particles are shown in Fig. 2.15. The catalytic activity of MoS_2 particles for the hydrodesulfurization of thiophene was higher than that of conventional MoS_2.

When polymer was used as an organic template, the polymer can be removed by thermal treatment. When an inorganic salt as NaCl was used as a template for the synthesis of carbon sphere, NaCl in the matrix can be removed by simple water washing [51]. Recently, hollow carbon spheres and porous carbon spheres can be prepared from aqueous solution including titanium(IV) bis(ammonium lactato) dihydroxide under air [52]. These spheres could be applied to electrode materials or stem cell engineering. Oxidation-resistant Cu–Sn particles can be prepared from aqueous solutions containing $Cu(NO_3)_2$, $SnCl_2$, and EG under N_2 [53]. Cu–Sn particles have a potential to be applied to the alternative material of silver in inks in printed electronics.

References

1. K.S. Suslick, S.-B. Choe, A.A. Cichowlas, M.W. Grinstaff, Sonochemical synthesis of amorphous iron. Nature **353**, 414–416 (1991)
2. K.S. Suslick, M. Fang, T. Hyeon, Sonochemical synthesis of iron colloids. J. Am. Chem. Soc. **118**, 11960–11961 (1996)
3. K.S. Suslick, T. Hyeon, M. Fang, Nanostructured materials generated by high-intensity ultrasound: sonochemical synthesis and catalytic studies. Chem. Mater. **8**, 2172–2179 (1996)
4. A. Comazzi, C. Pirola, M. Longhi, C.L.M. Bianchi, K.S. Suslick, Fe-based heterogeneous catalysts for the Fischer-Tropsch reaction: sonochemical synthesis and bench-scale experimental tests. Ultrason. Sonochem. **34**, 774–780 (2017)
5. X. Cao, Y. Koltypin, R. Prozorov, G. Kataby, A. Gedanken, Preparation of amorphous Fe_2O_3 powder with different particle sizes. J. Mater. Chem. **7**, 2447–2451 (1997)
6. N. Enomoto, S. Hirata, M. Inada, K. Hayashi, Crystallization behavior of iron-based amorphous nanoparticles prepared sonochemically. Ultrason. Sonochem. **35**, 563–568 (2017)
7. S.A. Yeung, R. Hobson, S. Biggs, F. Grieser, Formation of gold sols using ultrasound. J. Chem. Soc. Chem. Commun. **1993**, 378–379 (1993)
8. Y. Nagata, Y. Mizukoshi, K. Okitsu, Y. Maeda, Sonochemical formation of gold particles in aqueous solution. Radat. Res. **146**, 333 (1996)
9. R.A. Caruso, M. Ashokkumar, F. Grieser, Sonochemical formation of gold sols. Langmuir **18**, 7831 (2002)
10. K. Okitsu, A. Yue, S. Tanabe, H. Matsumoto, Y. Yobiko, Y. Yoo, Sonolytic Control of rate of Gold(III) reduction and size of formed gold nanoparticles in an aqueous solution: relation between reduction rates and sizes of formed nanoparticles. Bull. Chem. Soc. Jpn. **75**, 2289 (2002)
11. K. Okitsu, I. Kurisaka, B. Nanzai, N. Takenaka, H. Bandow, Sonochemistry of $NaAuCl_4$ aqueous alcohol solutions with C3–C6 alcohols under a noble gas atmosphere. Ultrason. Sonochem. **41**, 397–403 (2018)
12. K. Okitsu, H. Bandow, Y. Maeda, Y. Nagata, Sonochemical preparation of ultrafine palladium particles. Chem. Mater. **8**, 315 (1996)

13. K. Okitsu, Y. Mizukoshi, H. Bandow, Y. Maeda, T. Yamamoto, Y. Nagata, Formation of noble metal particles by ultrasonic irradiation. Ultrason. Sonochem. **3**, S249 (1996)
14. K. Okitsu, M. Ashokkumar, F. Grieser, Sonochemical synthesis of gold nanoparticles in water: effects of ultrasound frequency. J. Phys. Chem. B **109**, 20673 (2005)
15. Y. Mizukoshi, T. Fujimoto, Y. Nagata, R. Oshima, Y. Maeda, Characterization and catalytic activity of core-shell structured gold/palladium bimetallic nanoparticles synthesized by the sonochemical method. J. Phys. Chem. B **104**, 6028–6032 (2000)
16. Y. Nagata, Y. Watanabe, S. Fujita, T. Dohmaru, S. Taniguchi, Formation of colloidal silver in water by ultrasonic irradiation. J. Chem. Soc. Chem. Commun. **1992**, 1620–1622 (1992)
17. K. Okitsu, Y. Mizukoshi, H. Bandow, T.A. Yamamoto, Y. Nagata, Y. Maeda, Synthesis of palladium nano-particles with interstitial carbon by sonochemical reduction of tetrachloropalladate(II) in aqueous solution. J. Phys. Chem. B **101**, 5470–5472 (1997)
18. K. Okitsu, M. Murakami, S. Tanabe, H. Matsumoto, Catalytic behavior of Au Core/Pd shell nanoparticles on silica prepared by sonochemical and sol-gel processes. Chem. Lett. **29**, 1336–1337 (2000)
19. Y. Mizukoshi, E. Takagi, H. Okuno, R. Oshima, Y. Maeda, Y. Nagata, Preparation of platinum nanoparticles by sonochemical reduction of the Pt(IV) ions: role of surfactants. Ultrason. Sonochem. **8**, 1–6 (2001)
20. K. Okitsu, A. Yue, S. Tanabe, H. Matsumoto, Sonochemical preparation and catalytic behavior of highly dispersed palladium nanoparticles on alumina. Chem. Mater. **12**, 3006–3011 (2000)
21. Y. Mizukoshi, K. Okitsu, T. Yamamoto, R. Oshima, Y. Nagata, Y. Maeda, Sonochemical preparation of bimetallic nanoparticles of gold/palladium in aqueous solution. J. Phys. Chem. B **101**(36), 7033–7037 (1997)
22. A. Abulizi, G.H. Yang, K. Okitsu, J.-J. Zhu, Synthesis of MnO_2 nanoparticles from sonochemical reduction of MnO_4^- in water under different pH conditions. Ultrason. Sonochem. **21**, 1629–1634 (2014)
23. K. Okitsu, M. Iwatani, K. Okano, M.H. Uddin, R. Nishimura, Mechanism of sonochemical reduction of permanganate to manganese dioxide in aqueous alcohol solutions: reactivities of reducing species formed by alcohol sonolysis. Ultrason. Sonochem. **31**, 456–462 (2016)
24. K. Okitsu, K. Sharyo, R. Nishimura, One-pot synthesis of gold nanorods by ultrasonic irradiation: the effect of pH on the shape of the gold nanorods and nanoparticles. Langmuir **25**, 7786–7790 (2009)
25. K. Okitsu, Y. Nunota, One-pot synthesis of gold nanorods via autocatalytic growth of sonochemically formed gold seeds: the effect of irradiation time on the formation of seeds and nanorods. Ultrason. Sonochem. **21**, 1928–1932 (2014)
26. E.C. Dreaden, A.M. Alkilany, X. Huang, C.J. Murphy, M.A. El-Sayed, The golden age: gold nanoparticles for biomedicine. Chem. Soc. Rev. **41**, 2740–2779 (2012)
27. H. Chen, L. Shao, Q. Li, J. Wang, Gold nanorods and their plasmonic properties. Chem. Soc. Rev. **42**, 2679–2724 (2013)
28. H.S. Nam, J.K. Yoon, J.M. Ko, J.D. Kim, Electrochemical capacitors of flower-like and nanowire structured MnO_2 by a sonochemical method. Mater. Chem. Phys. **123**, 331–336 (2010)
29. S. Guo, S. Dong, Graphene nanosheet: synthesis, molecular engineering, thin film, hybrids, and energy and analytical applications. Chem. Soc. Rev. **40**, 2644–2672 (2011)
30. A. Abulizi, K. Okitsu, J.-J. Zhu, Ultrasound assisted reduction of graphene oxide to graphene in L-ascorbic acid aqueous solutions: kinetics and effects of various factors on the rate of graphene formation. Ultrason. Sonochem. **21**, 1174–1181 (2014)
31. D. Li, M.B. Muller, S. Gilje, R.B. Kaner, G.G. Wallace, Processable aqueous dispersions of graphene nanosheets. Nat. Nanotechnol. **3**, 101–105 (2008)
32. C. Zhu, S. Guo, Y. Fang, S. Dong, Reducing sugar: new functional molecules for the green synthesis of graphene nanosheets. ACS Nano **4**, 2429–2437 (2010)
33. L.M. Viculis, J.J. Mack, R.B. Kaner, A chemical route to carbon nanoscrolls. Science **299**, 1361 (2003)

34. U. Khan, A. O'Neill, M. Lotya, S. De, J.N. Coleman, High-concentration solvent exfoliation of graphene. Small **6**, 864–871 (2010)
35. M. Lotya, P.J. King, U. Khan, S. De, J.N. Coleman, High-concentration surfactant-stabilized graphene dispersions. ACS Nano **4**, 3155–3162 (2010)
36. L.-P. Jiang, S. Xu, J.-M. Zhu, J.-R. Zhang, J.-J. Zhu, H.-Y. Chen, Ultrasonic-assisted synthesis of monodisperse single-crystalline silver nanoplates and gold nanorings. Inorg. Chem **43**, 5877–5883 (2004)
37. Xu Hangxun, Kenneth S. Suslick, Sonochemical preparation of functionalized graphenes. J. Am. Chem. Soc. **133**, 9148–9151 (2011)
38. C. Wu, B.P. Mosher, T. Zeng, Rapid synthesis of gold and platinum nanoparticles using metal displacement reduction with sonomechanical assistance. Chem. Mater. **18**, 2925–2928 (2006)
39. C. Wu, B.P. Mosher, T. Zeng, Chemically-mechanically assisted synthesis of metallic and oxide nanoparticles in ambient conditions. J Nanoscience Nanotechnology **8**, 386–389 (2008)
40. J.-J. Zhu, S.T. Aruna, Y. Koltypin, A. Gedanken, A novel method for the preparation of lead selenide: pulse sonoelectrochemical synthesis of lead selenide nanoparticles. Chem. Mater. **12**, 143–147 (2000)
41. Q. Shen, Q. Min, J. Shi, L. Jiang, J.-R. Zhang, W. Hou, J.-J. Zhu, Morphology-controlled synthesis of palladium nanostructures by sonoelectrochemical method and their application in direct alcohol oxidation. J. Phys. Chem. C **113**, 1267–1273 (2009)
42. Y.-C. Liu, H.-T. Lee, H.-H. Peng, New pathway for sonoelectrochemical synthesis of gold–silver alloy nanoparticles from their bulk substrates. Chem. Phys. Lett. **400**, 436–440 (2004)
43. J.-J. Shi, S. Wang, T.-T. He, E.S. Abdel-Halim, J.-J. Zhu, Sonoelectrochemical synthesis of water-soluble CdTe quantum dots. Ultrason. Sonochem. **21**, 493–498 (2014)
44. K. Zhang, S. Yao, G. Li, Y. Hu, One-step sonoelectrochemical fabrication of gold nanoparticle/carbon nanosheet hybrids for efficient surface-enhanced Raman scattering. Nanoscale **7**, 2659–2666 (2015)
45. S.K. Mohapatra, M. Misra, V.K. Mahajan, K.S. Raja, A novel method for the synthesis of titania nanotubes using sonoelectrochemical method and its application for photoelectrochemical splitting of water. J. Catal. **246**, 362–369 (2007)
46. R.J. Lang, Ultrasonic atomization of liquids. J. Acoust. Soc. Am. **34**, 6–9 (1962)
47. B. Xia, I.W. Lenggoro, K. Okuyama, Novel route to nanoparticle synthesis by salt-assisted aerosol decomposition. Adv. Mater. **13**, 1579–1582 (2001)
48. B. Xia, I.W. Lenggoro, K. Okuyama, Nanoparticle separation in salted droplet microreactors. Chem. Mater. **14**, 2623–2627 (2002)
49. Y.T. Didenko, K.S. Suslick, Chemical aerosol flow synthesis of semiconductor nanoparticles. J. Am. Chem. Soc. **127**, 12196–12197 (2005)
50. S.E. Skrabalak, K.S. Suslick, Porous MoS_2 synthesized by ultrasonic spray pyrolysis. J. Am. Chem. Soc. **127**, 9990–9991 (2005)
51. Sara E. Skrabalak, Kenneth S. Suslick, Porous carbon powders prepared by ultrasonic spray pyrolysis. J. Am. Chem. Soc. **128**, 12642–12643 (2006)
52. W.H. Suh, J.K. Kang, Y.-H. Suh, M. Tirrell, K.S. Suslick, G.D. Stucky, Porous Carbon produced in air: physicochemical properties and stem cell engineering. Adv. Mater. **23**, 2332–2338 (2011)
53. Y. Liang, H. Hou, Y. Yang, H. Glicksman, S. Ehrman, Conductive one- and two-dimensional structures fabricated using oxidation-resistant Cu–Sn particles. ACS Appl. Mater. Interfaces. **9**, 34587–34591 (2017)

Chapter 3
Synthesis of Micro-nanoparticles Using Ultrasound-Responsive Biomolecules

Abstract The ultrasonic crosslinking of biomacromolecules and biomolecules can be exploited to fabricate micro-nanodevices. In particular, biologically relevant molecules and macromolecules are desirable building blocks for engineering biomaterials. Ultrasonic synthesis, modification, and assembly of biomolecules and biomacromolecules enable the tuning of size, composition, degradability, surface properties, and biofunctionality of micro-nanodevices. Recent achievements in engineering of micro-nanodevices using ultrasound-responsive biomolecules such as proteins, amino acids, and phenolic molecules will be discussed in this section. These recent findings highlight the potential use of high- and low-frequency ultrasound techniques to fabricate innovative platforms for biomedical applications.

Keywords Protein-shelled microbubbles · Phenols oligomerization · Tyrosine oligomerization · Self-assembly of phenolics

3.1 Introduction

Ultrasound has been successfully used for different radical mediated coupling reactions between organic molecules. Conventional-free radical emulsion polymerization involves an insoluble monomer dispersed in an aqueous phase [1, 2] and typically water-soluble chemical initiator should be present. The initiator is then treated, either thermally, photochemically, or via a redox reaction to generate active free radicals [2]. Free radical emulsion polymerization using ultrasound has been reported previously [3]. Different polymers have been prepared by using ultrasound and monomers such as styrene [4–6], methyl methacrylate [7–10], and butyl acrylate [7, 10]. Biggs and Grieser [4] have studied the sonochemical polymerization of styrene in water emulsions without the addition of any chemical initiator. Similarly, synthesis of butyl acrylate/vinyl acetate copolymer latex nanoparticles using ultrasound as a polymerization initiation source was carried out to produce particles with

Sukhvir Kaur Bhangu, Enrico Colombo and Muthupandian Ashokkumar contributed to this chapter.

K. Okitsu et al., *Sonochemical Production of Nanomaterials*,
Ultrasound and Sonochemistry, https://doi.org/10.1007/978-3-319-96734-9_3

narrow particle size distribution as compared to conventional process [2]. Bradley and Grieser [11] have examined the mechanism involved in the synthesis of poly(methyl methacrylate) and poly(butyl acrylate). They have suggested that initiation of polymerization occurred through the generation of monomer radicals in the emulsion system. The H/OH radicals produced as a result of homolysis of water can undergo addition to monomer molecules adsorbed at the bubble–solvent interface leading to the formation of monomeric radicals providing an alternative pathway to initiate the polymerization. Radicals generated by acoustic cavitation can be also used for coupling reactions between biomolecules, taking place at the air–liquid interface. In particular, biomolecules and biopolymers bearing thiols and phenolic groups are sensitive to ultrasound and can be easily modified and assemble into nanostructured systems. The ultrasonic crosslinking of proteins has been exploited in the synthesis of lysozyme air-filled microbubbles and oil-filled microcapsules [12]. The ultrasonic crosslinking of thiolated synthetic polymer such as polymethacrylic acid was also reported to occur at the air–water and oil–water interfaces. Upon sonication, new intermolecular disulphide linkages were formed by HO_2 radicals leading to the formation of stable gas-filled and oil-filled micro-nanoparticles with a high degree of control over size, polydispersity, and shell thickness [13, 14]. Recent achievements in engineering of micro-nanodevices using ultrasound-responsive biomolecules such as proteins, amino acids, and phenolic molecules will be discussed in this section. These recent findings highlight the potential use of high- and low-frequency ultrasound techniques to fabricate innovative platforms for biomedical application.

3.2 Ultrasonic Synthesis and Assembly of Protein-Shelled Microbubbles and Microcapsules

In the last decade, Cavalieri et al. [13, 14] developed an ultrasonic method to synthesize and characterize stable air-filled microparticles, i.e., microbubbles (MB) and microcapsules (MC), using lysozyme (Fig. 3.1). Hen egg-white lysozyme has been widely studied and proven to have pharmacological and therapeutic applications with a low molecular weight (14 kDa) protein, and it contains four intramolecular disulphide bonds. The disulphide bonds can be partly broken using reducing agents, such as dithiothreitol (DTT) (Fig. 3.1). High-intensity ultrasound (20 kHz microtip horn with 3 mm diameter) has been used to synthesize lysozyme air-filled microbubbles with controlled size and polydispersity. Prior applying the ultrasound the lysozyme solution was chemically denatured.

Upon sonication, HO_2 radicals are generated due to the cavitation process which helps to form new intermolecular disulphide linkages leading to the formation lysozyme MBs with a thick and elastic (150–200 nm) protein shell. The mechanism involved in the formation of air-filled microbubbles is emulsification and cavitation which are induced by ultrasound (Fig. 3.1). The collapse intensity of cavitation bubbles influences the shear forces, which are responsible for emulsification. HO_2

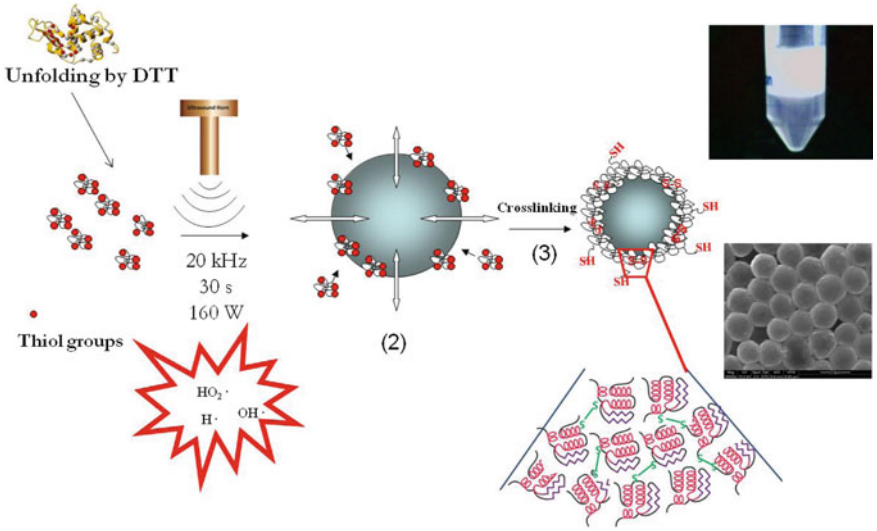

Fig. 3.1 Schematic illustration showing the lysozyme-shelled MB preparation technique, the shell structure, and the resulting MB in suspension and dry state

radicals generated as a result of cavitation induce crosslinking between protein aggregates. An increase in ultrasonic power leads to an increase in shear forces and radical yield, which result in effective crosslinking of lysozyme and stabilization of gas bubbles. The size and size distribution of microbubbles can be controlled by alteration ultrasonic parameters and post-treatment of microbubble suspension [15].

In addition, lysozyme-shelled microcapsules (MC) can be generated at water–perfluorohexane interface using ultrasound [14]. The perfluorocarbon (PFC) and gas-filled microparticles are suitable for ultrasound contrast agents in different clinical applications [16]. The MBs and PFC microcapsules (MCs) bear echogenic properties in biological tissues due to their acoustic impedance being similar to the blood and solid tissue. Interestingly, it has been demonstrated that the denatured lysozyme arrangement differs depending upon the chemical nature of interface. Changes in the arrangement of lysozyme at different interfaces effect both conformation and bioactivity of the protein. A comparison between the physicochemical and functional properties of lysozyme MBs and MCs suggests a different mechanism of formation. The size of microcapsules and microbubbles was determined using optical and scanning electron microscope and was found to be about 2.5 μm for both MBs and MCs. On the other hand, residual thiol content in MB shell was significantly higher (62 mmol mg^{-1}) than that of MC shell (12 mmol mg^{-1}). Circular dichroism (CD) was used to evaluate the secondary structure of protein in MBs and MCs. CD spectra showed the transition of native-like conformation to a secondary structure rich in β-sheets in case of MBs; however, in case of MCs, both helical and β-sheets contents were increased. The degradation of MBs and MCs by a protease was assessed, and

due to the access protease to the polypeptide chain lysozyme (denatured) in MBs was more prone to degradation than in MCs. In addition to this, no amyloid-like fibrils formation within the lysozyme shell was observed. The isoelectric point of lysozyme is 10; therefore, the ζ-potential values for both MBs and MCs in Milli-Q water were +29 mV and +32 mV, respectively. The positively charged surface acts as template for the assembly of protein present in blood and cell culture medium which are usually negatively charged and such interactions help to control the biological response of MBs and MCs. Bovine serum albumin showed fast and strong association with both the microparticles as the ζ-potentials of MBs and MCs were -24 ± 8 mV and -30 ± 3 mV, respectively, after the incubation of MBs and MCs with BSA showing the adsorption protein on the microparticle surface due to the electrostatic, hydrophobic, and thiols interactions. Apart from this, lysozyme is found to be effective antimicrobial agent [17]; therefore, the antimicrobial activities of MBs and MCs were also investigated by observing the disruption of *Micrococcus lysodeikticus* cell wall. MBs possess significant antimicrobial activity, whereas MCs do not show any antimicrobial activity. It has been reported that partially unfolded lysozyme can act as a potent bactericidal agent against both Gram-negative (*Escherichia coli*) and Gram-positive (*Staphylococcus aureus, Micrococcus luteus*) bacteria irrespective to its enzymatic muramidase activity [17]. The antimicrobial activity of MBs can be due to a residual muramidase activity and hydrophobic moieties on the surface subjected to the protein crosslinking and unfolding. The hydrophobic surface can enhance the interactions between microbubbles and bacterial membrane disturbing its functioning and integrity. The lack of antimicrobial activity in MCs is therefore ascribed to the more hydrophilic bubble's surface.

3.2.1 The Echogenic Properties of Lysozyme Microbubbles

Currently, MBs are used clinically as ultrasound contrast agents for ultrasound myocardial perfusion imaging [18] and focal liver lesion diagnosis and have been approved for the detection of focal breast lesions recently. In the last decades, MBs have been widely investigated for the innovative therapeutic interventions [19]. Therefore, ultrasound is an attractive tool for a drug delivery modality. Ultrasonic method is cost-effective and accessible to internal organs, and lacks the use of any ionizing irradiation (in contrast to CT/PET). The irradiation of tissue is feasible with ultrasound and the ultrasonic beam can be directed to the different deeply located body sites with millimeter precision [16]. MBs can be suitable for the ultrasonically enhanced local drug delivery as they can be concentrated and disrupted at the acoustic field regions selectively. MBs administered can also intravenously circulate in the bloodstream and accrued in the region of interest [20]. Alternatively, MBs can be also administrated locally. The drug-loaded MBs and their ultrasound triggered disruption can provide controlled release and admiration of drug limited to the site of application. In order to exert the diagnostic and therapeutic role, microbubbles physical properties must be characterized. The physicochemical stability of microbubbles must be controlled and tuned depending on the specific application.

The MBs are shown to have high scattering intensity per particle as compared to other contrast agents. The ultrasonic intensity scattered by spherical particle smaller than the wavelength of irradiation can be determined by Eq. 3.1, which describes Rayleigh scattering regime [21],

$$\frac{I}{I_0} = \frac{1}{9}\frac{k^4 r^4(\gamma_c + \gamma_d \cos\theta)^2}{d^2} \tag{3.1}$$

where I is the scattered intensity, I_0 is the incident intensity, k is the wave number, r is the radius of the particle, γ_c is the compressibility term, γ_d is the density term, θ is the scattering angle equal to 180° for backscattering, and d is the distance from scattering object. The compressibility and density terms can be determined from $\gamma_c = (k_s - k_m)/k_m$, (where k_s and k_m are the compressibility of the scattering object and the medium, respectively) and $\gamma_d = (3\rho_s - 3\rho_m)/(2\rho_s + \rho_m)$, ($\rho_s$ and ρ_m are the densities of the scattering object and the medium, respectively). The gaseous particles exhibit very high compressibility as compared to solids and liquids so thus is their scattering efficiency. Along with the Rayleigh scattering (the intensity of which increases as the fourth power of frequency), MBs tend to resonate at the intrinsic resonant frequency f_0. For a gas bubble in water, f_0 can be determined by the Eq. 3.2:

$$f_0 = \frac{1}{2\pi r}\left(\frac{3\gamma p_{\text{atm}}}{\rho}\right) \tag{3.2}$$

where r is the radius of the bubble, p_{atm} is the atmospheric pressure, ρ is the density of water, and ρ is the ratio of specific heats of the gas. It is known that for intravenous injection the size of the microbubbles plays a significant role, and therefore it must be carefully controlled. Due to the dependence of intensity on size, the small bubbles are less effective to scatter ultrasound whereas large bubbles are not able to pass through the capillaries. It has been reported and approved that the size needs to be in the range of 1–7 μm with a narrow size distribution.

Apart from this, different types of physical and biological effects have been observed due to the absorption of acoustic energy by the bubbles. Upon ultrasound exposure, MBs will first grow in volume and then implode violently. Acoustic streaming, thermal effects, and highly reactive free radicals accompany acoustic cavitation. Despite the extensive use of MBs in diagnostics, the therapeutic use of the cavitation effects generated by the interaction between MBs and ultrasound in the in vivo circulatory system is still under investigation.

The MI value can be determined by using Eq. 3.3, and it is a value that estimates the probability of an adverse mechanical biological effect on a tissue exposed to diagnostic ultrasound. If the MI value is ≥1, then the probability of bioeffects is higher.

$$\text{MI} = \frac{\bar{p_{\text{ac}}}}{\sqrt{f}} \tag{3.3}$$

p_{ac}^{-} is the peak rarefaction acoustic pressure normalized by 1 MPa and f is the center frequency of the ultrasound normalized by 1 MHz.

The activity of bubble can occur at low and high acoustic amplitudes. MBs in capillary oscillate with small to moderate changes in the radius (Off-resonance regime). When the acoustic power is increased (MI > 0.6), bubbles experience nonlinear (asymmetric) oscillations with emission of harmonics of the fundamental (incidence) frequencies; therefore, it behaves as a source of sound, rather than as a passive reflector. MBs undergoing nonlinear oscillations can also inertially implode.

It is known that the biological tissue does not show such interactions with ultrasound, and thus they do not generate any harmonic frequencies; therefore, the acoustic signal generated can be exploited for imaging purposes. Due to the implosion, the bubble can fragment into number of smaller bubbles and it can be observed with contrast agents made from thin elastic shells [22, 23].

In addition, sonic cracking can occur by ultrasound leading to the formation of shell defects causing gas to escape from the MBs. Such behavior has been reported during insonification of rigid albumin-shelled MBs [24]. When the bubble is encapsulated with a biomacromolecules, the acoustic behavior of the bubble changes dramatically. The increase in the resonance frequency due to the shell stiffness and enhancement in damping due to the viscosity has been reported. For lysozyme MBs, the main mechanism for the bubble destruction was fragmentation. When the acoustic pressure is greater or equal to the fragmentation threshold, large-amplitude expansion and contraction of the MBs can damage the lightly crosslinked protein shells leading to the fragmentation of bubble into small pieces accompanied by the emission of broadband noise in the process [25]. Shockwave high-speed imaging of lysozyme MB was used to visualize the cracking of the crosslinked protein shell after application of shockwave pressure. Shockwave-induced dynamics was studied applying a peak positive pressure of 28 MPa and a peak negative pressure of about 6 MPa. The shockwave induces the shell cracking, and the expansion and compression of the free gas bubbles are recorded using high-speed camera (Fig. 3.2).

In addition to this, when a bubble is collapsed rapidly near a boundary, it can undergo asymmetric collapse; due to this, a high-speed liquid jet may project through the bubble toward the boundary. This phenomenon is termed as microjetting. Fragmentation, microjetting, and sonic cracking can act as effective mechanism for drug delivery; therefore, their occurrence should be finely predicted and tuned [20].

In order to determine the ultrasound backscattering ability of lysozyme-shelled microbubbles (LSMBs) for imaging purposes, a 10 MHz scanner has been used [26]. A phantom was used to mimic tissue structure, and a channel was made to flow the microbubble suspension through which lysozyme solution (1 mg mL^{-1}) was injected as a reference. The ultrasound probe at 10 MHz with a mechanical index (MI) at 0.36 was then used on the phantom. Figure 3.3a, d shows ultrasound scanning images, and it was observed that the channel with lysozyme solution appears as a black hole which shows that there is no backscattering signal from the solution. In contrast to this, pristine and gold-functionalized LSMBs show a bright and blue contrast within the hole (Fig. 3.3b, e) under the B-mode and Doppler mode (Fig. 3.3c, f).

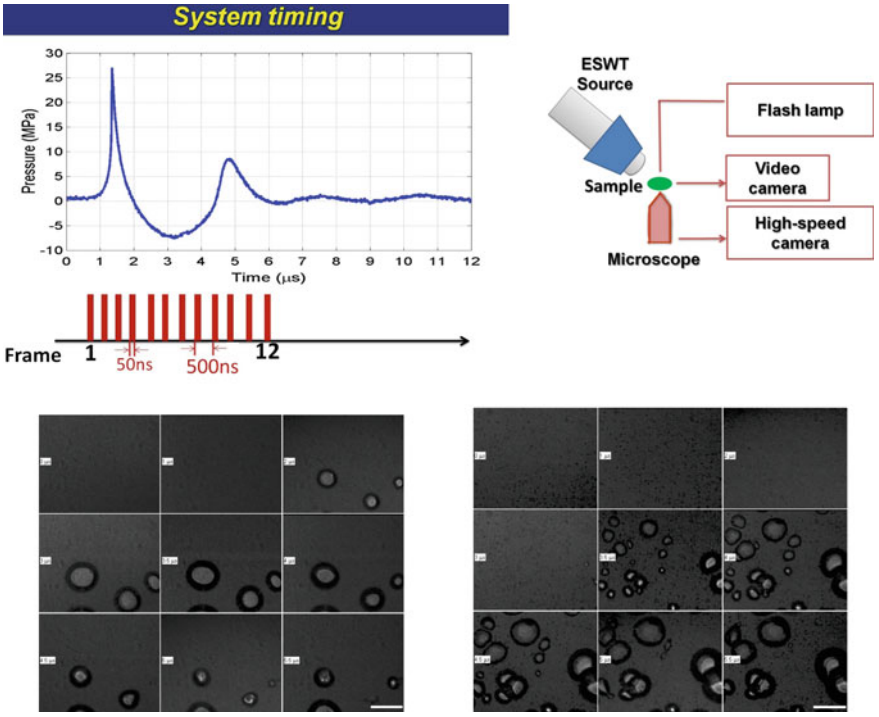

Fig. 3.2 Setup for high-speed imaging of shockwave-induced dynamics. Exposure time (50 ns), interframe rate (500 ns). The shockwave induces the shell cracking, and the expansion and compression of the free gas bubbles are recorded using high-speed camera (unpublished data)

It has been reported that to develop micro-antimicrobial and biosensing devices the LSMBs can be engineered as a support for the immobilization of gold nanoparticles, AuNPs, and an enzyme, alkaline phosphatase (AP), [26]. Air-filled lysozyme microbubbles functionalized with AuNPs exhibit significant bactericidal activity and echogenic properties. The conjugation of AP on microbubbles surface has been carried out to generate sensitive biosensor for the detection of analytes in aqueous solutions. For instance, functionalized microbubbles were used for the detection of paraoxon in aqueous solutions [27]. The mechanical properties of the shell of LSMBs were evaluated by a very recently introduced technique, the acoustic interrogation [28]. It was reported that the shell elasticity and Young's modulus are MBs size-independent, and Young's modulus of LSMBs was around 1.0 ± 0.3 MPa. These results suggest that due to the hydrogel-like protein shell of LSMBs, it can offer a soft, more elastic, and less viscous interface compared to lipid-shelled MBs.

Undoubtedly, the ultrasonic techniques offer a simple, safe, and fast route for synthesizing micro-nanospheres. In addition, the fundamental understanding gained from this research work was unquestionably important and advanced the knowledge base in the microbubbles research field. Although considerable advances have been

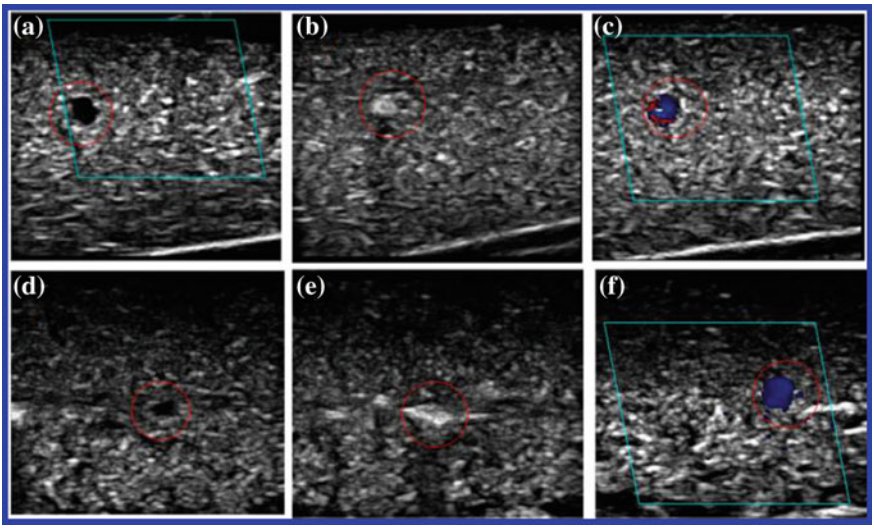

Fig. 3.3 Ultrasound scanning images of **a**, **d** lysozyme aqueous solution, **b**, **c** pristine LSMBs solution (in **b** B-mode and **c** Doppler mode), and **e**, **f** LSMBs functionalized with BSA-coated AuNPs (in **e** black mode and **f** color mode). Reproduced with permission from [26] Copyright 2013 American Chemical Society

made in this field with respect to the synthesis and characterization of biopolymer-shelled microparticles, there are still significant areas of the research that remain a challenge. For instance, in order to tune the structural and functional properties of micro-nanobubbles, the ultrasonic technique should be applied to other interesting proteins with suitable amphiphilic properties, synthetic biocompatible polymers bearing crosslinkable moieties, or mixture of protein and synthetic polymers to obtain hybrid and multifunctional systems.

3.3 Synthesis of Nanoparticles Using Ultrasound-Responsive Phenolic Molecules

The phenolic structures generated by polymerization of phenolic moieties in past few decades have gained attention due to their multipurpose nature. They are widely used in food and pharmaceutical industries. There are a number of different techniques which are used to carry out the polymerization of such molecules. The polymerization of 3-methylcatechol with the horseradish peroxides which can be used for germanium recovery [29]. It was proposed that radicals can be generated with HRP and H_2O_2 which are then transferred to the monomer followed by the monomer polymerization and precipitation. A study by Eker et al. [30] carried out the phenol formaldehyde resins have found many applications such as surface coating, adhesives, laminates,

etc. but due to the toxicity of formaldehyde, many countries have limited its use. Formaldehyde-free polymerization can be carried out using chemical catalysts such as copper and copper complexes. Another alternative is the use of enzymatic catalysts such as soybean peroxidase and horseradish peroxidase [30, 31]. Enzymatic polymerization using the templates like poly(ethylene glycol), poly(ethylene glycol) monododecyl ether has been carried out to synthesize the soluble polyphenols [32–34]. Alternatively, oxidative coupling reactions have been studied using the pulse radiolysis and Fenton-type reactions [35]. In another study, oxidative coupling of green tea polyphenol was performed by using copper (II) as a catalyst and the reaction was assisted by heat [36]. In addition to these methods, this reaction was induced by microwave irradiation and $AgNO_3$ leading to the formation of metal–tea polyphenol nanoparticles [37].

The oxidation of tyrosine-bearing proteins is also considered very important as it can help in understanding physiological and pathological processes involving protein crosslinking and aggregation [38]. Such reactions, i.e., formation of dimers, trimers, and oligomers of tyrosine in proteins, have been obtained by different biocatalysts, UV irradiation, pulse radiolysis, or inorganic catalysts [35, 38, 39].

On the other hand, a recent study by Cavalieri et al. [40] has utilized a different and innovative approach, where the radicals generated by acoustic cavitation were used for carrying out the oxidative coupling reactions and polymerize the phenolic moieties. It is well known that ultrasound can produce high temperature and pressure of the order 5000 k and 2000 atm, respectively, and radicals such as H, OH, NO, O, etc. along with some physical effects including microstreaming microjetting, shear forces, etc. [40–43]. Therefore, such effects can be utilized for carrying out a different inorganic, organic, and materials synthesis.

If the ultrasonication of phenolic moieties is considered, it has been reported many times with low as well as high frequency. Most of the reports have focused their attention on the degradation of phenol. For instance, they have reported the formation of intermediate products such as catechol, hydroquinone, ortho, and para quinone [44–48] but none of the studies have reported the formation of dimeric, trimeric, and oligomeric species.

Cavalieri et al. [40] and Bhangu et al. [49] have demonstrated that the phenolic and tyrosine derivatives can undergo a number of oxidative modifications upon high-frequency (0.35–1 MHz) ultrasound treatment. The products formed were hydroxylated molecules (hydroxylated tyrosine and phenolic moieties), dimers, trimers, and oligomers, which could self-assemble into fluorescent, monodisperse, and functional nanoparticles. Additionally, the same method was employed to crosslink tyrosine-bearing proteins, to form protein nanoparticles. The synthesis did not involve any assistance by coordination metal, but it used the catalytic role of reactive surfaces of cavitation bubbles. The work introduced a new strategy for the fabrication of nanoparticles, exploiting oxidative coupling of phenolic moieties without the use of metals or enzymes.

In the first study [40], to mimic tyrosine moieties in protein structures, *N*-benzoyl-*L*-tyrosine ethyl ester (BTTE) was utilized. In addition, the low solubility of BTEE in water (due to its high nonpolar nature) permitted a maximization of its diffusion to the

gas bubble/liquid interface during sonication. Nevertheless, the study on the simple phenolic molecules further confirmed that it is not only the hydrophobicity but also the ionic strength deriving the reaction, concentration, and the surface activity of the solute molecules which play important role in promoting such coupling reactions. As a source of ultrasonic waves for the formation of radicals, a transducer plate able to operate at a frequency of 355 or 1000 kHz was used. Typically, a 1 mM BTEE solution (in water) and 0.5–10 mM phenol solution (in PBS pH = 7) was treated under ultrasonic irradiation for up to 6 h at 37 °C. To monitor the conversion of BTEE and phenol to the products formed during the sonication, RP-HPLC, mass spectrometry (MS), and fluorescence spectroscopy were utilized.

Figure 3.4 shows the RP-HPLC chromatograms and MS analysis results, collected during the sonication of BTEE during the ultrasonic treatment, for a total time of 3 h. After 3 h of ultrasonic irradiation, BTEE was almost totally converted into BTTE oxidized species and higher molecular weight dimers and oligomers (Fig. 3.4a and b). The identification of the peaks in the RP-HPLC chromatogram was possible due to its comparison with the MS analyses. Particularly, the mass spectra collected after 0.5 h of sonication (Fig. 3.4c) shows the presence of oxidation products. In details, the peaks at 330, 665, and 681 m/z indicate the presence of OH-BTEE, OH-BTEE/BTTE dimers, and OH-BTEE/OH-BTTE dimers, respectively. After 1 h of irradiation (whether the ultrasonic frequency was 355 or 1000 kHz), the solution became turbid and a sample was analyzed by SEM (Fig. 3.4e), which showed the formation of nanoparticles. Addition of an organic solvent (e.g., acetonitrile) permitted a return to a clear solution confirming that the nanoparticles formed were the result of nonpolar interactions. Moreover, nanoparticles dissolution permitted to perform MS analyses (Fig. 3.4d), which showed the presence of high-molecular-weight species. In details, in the range of 850–1600 m/z, multiple peaks were observed. Those peaks were associated with oligomers composed by 4–5 OH-BTTE repeating units. With the growth of the molecular weight, the solubility of the oligomers decreased, leading to a self-assembled spherical nanostructure.

After 3 h of ultrasonic irradiation at 355 kHz, the colloidal nanoparticles were collected by centrifugation, washed several times with Milli-Q water and dried at 80 °C overnight, showing a final yield of about 40%. Similar results were obtained with phenol sonication in PBS (pH = 7) where the phenol was converted into catechol, benzoquinone, hydroquinone, and different high-molecular-weight species (dimers, trimers, and oligomers) which was also confirmed by mass spectrometry and HPLC [49]. The formation of conjugated aromatic structures in case of phenol was also confirmed from an increase in the absorption intensity in the range of 300–800 nm which is due to the conjugation of aromatic rings [50, 51].

To corroborate the data collected by RP-HPLC, MS, and SEM, and to shed light on the phenol and BTTE oxidation and coupling reactions, fluorescence spectroscopy analyses were performed over a period of 6 h (Fig. 3.5).

Fluorescence emission is influenced by the pH of the medium. To avoid variation due to differences in pH, the analyses were performed dispersing a small aliquot of sample (40 μL) into a PBS (pH 7.4) buffer solution (final total volume 3 mL). Figure 3.5a shows the fluorescence emission as a function of time. The emission peak

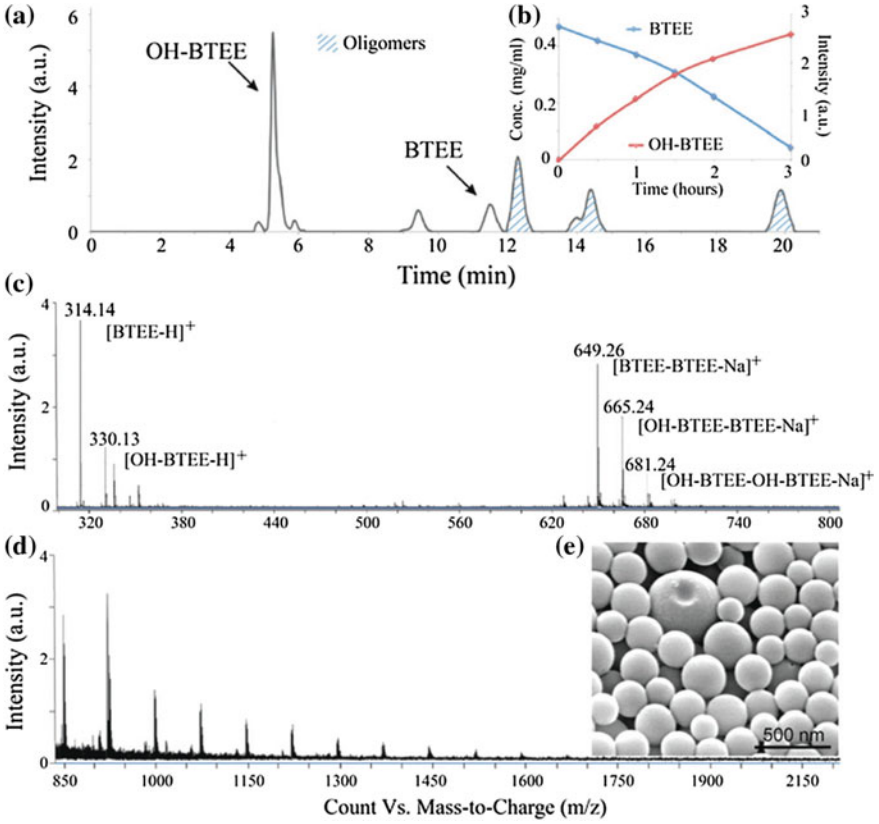

Fig. 3.4 RP-HPLC, MS, and SEM analyses of BTEE sonicated at 355 kHz. **a** HPLC chromatogram of BTEE after 30 min of sonication; **b** concentration of BTTE against the signal intensity of OH-BTEE as a function of sonication time; **c** MS spectra of BTTE after 30 min of sonication; **d** MS of the BTEE oligomer nanoparticles produced after three hours of sonication and dissolved in acetonitrile; and **e** SEM images of nanoparticles obtained during sonication after separation by centrifugation and several washing with Milli-Q water. Reproduced with permission from [40] with permission from The Royal Society of Chemistry

is centered at 420 nm, and its intensity increases over the period analyzed. Additionally, a clear redshifted is observable, with the maximum intensity shifting to 446 nm after 6 h of sonication. This type of shifting indicates that different fluorescent species were formed during the ultrasonic irradiation of BTTE, with the final emission peak being the sum of the emissions of all the fluorescent species. Phenolic, catecholic compounds, and o-quinones do not exhibit fluorescence in this region. It has been reported that only tyrosine–tyrosine and phenolic dimers exhibit fluorescence in the 400–500 nm spectral range, when excited within 320 and 380 nm, which originates from the conjugated system and the phenolate form of the excited single state

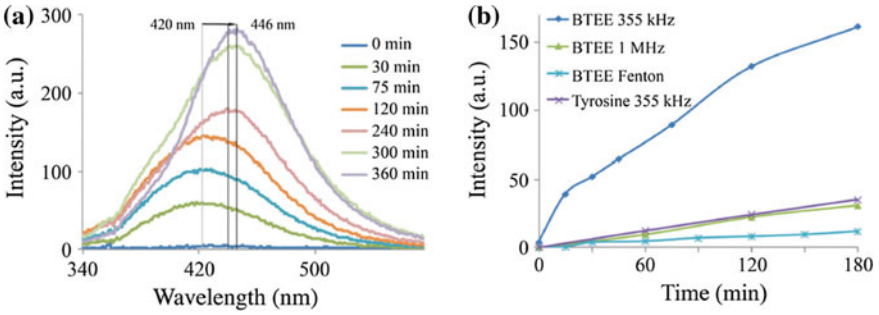

Fig. 3.5 **a** The fluorescence emission spectra (λex 320 nm) of BTTE oxidation products formed during sonication at 355 kHz and **b** peak fluorescent emission over time arising from BTEE samples sonicated at 355 and 1000 kHz, using tyrosine at 355 kHz and using BTEE with radicals generated by the Fenton reaction. Reproduced from [40] with permission from The Royal Society of Chemistry

[52, 53]. On the other hand, during the phenol sonication, the fluorescent peak appeared at 360–370 nm after 30-min sonication slowly decreased with a concomitant increase in the peak at 446 nm (Fig. 3.5a). The peak at 360–370 nm was ascribed to the dimer as the spectral profile was similar to the 2,2-biphenol, whereas the fluorescence peak at 446 nm was due to high-molecular-weight oligomers. Similar redshift from 446 to 478 nm depending upon the excitation wavelength was also observed in the sonicated phenol confirming the formation of different oligomeric products.

Figure 3.6b shows the fluorescence emission in PBS buffer overtime for four different reaction conditions: BTEE sonicated at 355 (used as a reference) and 1000 kHz, BTEE oxidized using Fenton reaction, and tyrosine ultrasonically irradiated at 355 kHz. In all cases, the fluorescence spectra observed were similar to that observed in the 355 kHz irradiated samples of BTEE, confirming the formation of dimers and oligomers.

The authors compared the reaction occurring by OH radicals with and without the assistance of ultrasound to shed light on the role of the cavitation bubble. The fluorescent emission of the species obtained using 355 kHz ultrasound was compared to that of the species obtained using a Fenton reaction (Fig. 3.5a). An equivalent amount of radicals was used in the Fenton reaction to simulate the amount of radicals generated by ultrasound. However, the Fenton reaction did not show a relevant formation of phenol and BTEE dimers and, suggesting that the radicals alone are not responsible for the generation of such species, the surface of the cavitation bubble must have a catalytic role in promoting the coupling of different nonresponsive molecules. Indeed, tyrosine exhibits a lower nonpolar behavior compared to that of BTEE, resulting in a lower amount of tyrosine molecules migrating on the gas bubble/liquid interphase when sonicated under the similar conditions.

However, in case of phenol sonicated at 1000 kHz, the fluorescence spectral profile showed only one peak at 370 nm which was attributed to the formation of dimers

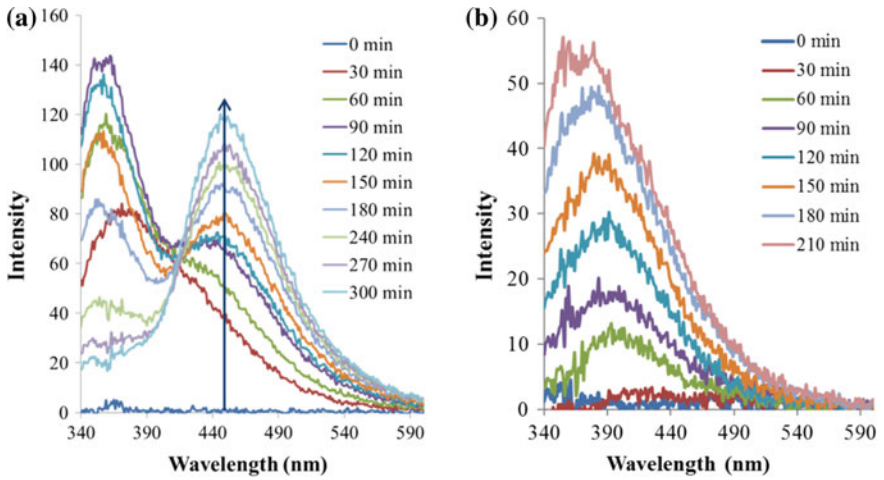

Fig. 3.6 The fluorescence emission spectra (λex 320 nm) of phenol oxidation products formed during sonication at **a** 355 kHz and **b** 1000 kHz. Reproduced with permission from [49], Copyright 2016 American Chemical Society

(Fig. 3.6b). Once the sonication was ceased, the authors observed a leveling off in the enhancement of the fluorescence, confirming that the radicals produced during the acoustic cavitation were responsible for the BTEE and phenol oxidation and coupling reactions.

The study carried out by Cavalieri et al. [40] and Bhangu et al. [49] investigated the effect of different sonication frequencies on the coupling reactions. The ultrasound-assisted coupling reactions were carried out at 20, 355, and 1000 kHz. They observed that at 20 kHz, only 10% of BTEE was dimerized after 3 h of ultrasonic irradiation and phenol did not show any dimerization or oligomerization. Results collected after sonication at 355 and 1000 kHz are shown in Fig. 3.6b, suggesting that the optimal frequency for the occurrence of coupling reactions is 355 kHz. This effect was associated with two main reasons: quantity of radicals produced and length of bubble life cycle. When ultrasound is used, the concentration of radicals generated grows from 20 to about 350 kHz where a maximum is reached and further decreases at higher sonication frequencies. For instance, an increase in ultrasonic frequency from 350 to 1000 kHz results in a threefold decrease in the OH radicals generated. This behavior is due to a shorten in the bubble life cycle, which results in a smaller amount of vapor entering the bubble during the expansion phase of the acoustic cycle [43, 54]. As a result, less radicals can be produced, which is consistent with the smaller number of dimers produced when BTEE and phenol were sonicated at 1000 kHz (Fig. 3.5b and 3.6b). However, the reduction is smaller than a threefold decrease, which suggested that additional factors were playing a role in the coupling reactions. To explain this behavior, the authors proposed a mechanism for the coupling of tyrosine derivates (Scheme 3.1).

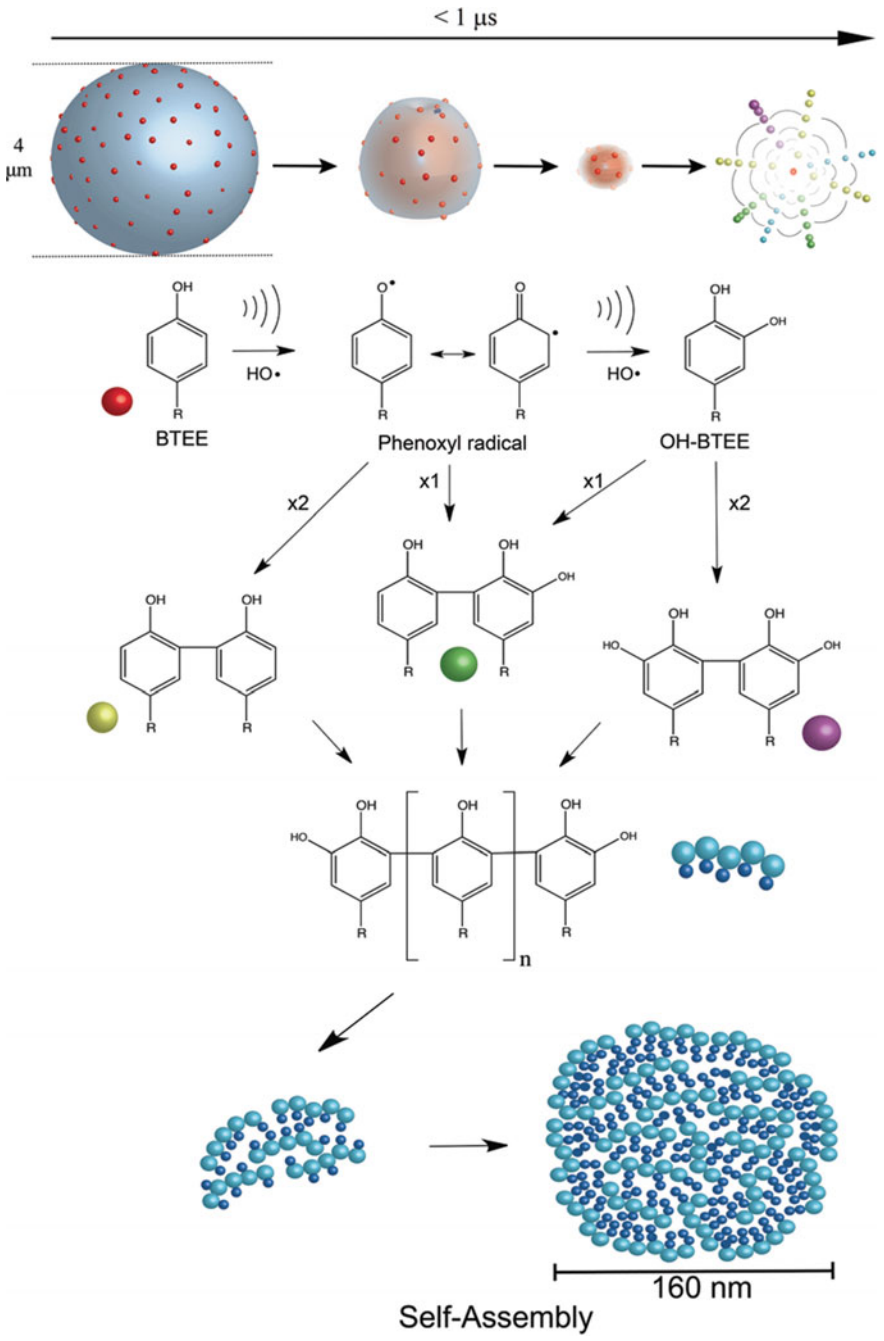

Scheme 3.1 Mechanism of the coupling reaction of phenolic or tyrosine moieties into hydroxylated species, oligomers, and sequential nanoparticles self-assembly. Reproduced from [40] with permission from The Royal Society of Chemistry

In the mechanism proposed by Cavalieri et al., the aromatic rings of the phenolic moieties should approach each other prior to their oxidation and sequential coupling. The diffusion coefficient for different amino acids spans from 7 to 10×10^{-10} m^2 s^{-1}, while the chemically active cavitation bubble exists for about 0.3–0.1 ms in the frequency range of 200–1000 kHz. This is a sufficient time for diffusion, adsorption, and reaction, of the phenol and BTEE molecules at the bubble/liquid interphase. Nonetheless, the faster the oscillation, the smaller the number of BTEE and phenol molecules able to migrate and adsorb on the oscillating bubble, resulting in a lower amount of coupling reaction occurring. Additionally, at 355 kHz, the higher the shear forces, as well as the higher temperatures, generated when the collapse of the bubble occurs might contribute in the acceleration of the coupling reaction of the tyrosine moieties. Once the initial dimerization occurs, the dimer formed resulted in being more hydrophobic than the monomer, resulting in a faster migration to the bubble/liquid interphase, ready to incur in additional coupling. As a result, oligomers start to be generated before the consumption of all the initial BTEE molecules. With phenol at 1 MHz, the formation of only dimer was observed (Fig. 3.6b); since, phenol is a small molecule and it has sufficient time to diffuse, absorb, and react at the interface of 1 MHz oscillating bubble to form dimers. However, dimeric species cannot reach the interface before bubbles collapse, and as a result the formation of other oligomeric species was not observed. Once a certain length and concentration are reached, the oligomers become insoluble in water, self-assembling in nanostructures. The nanoparticles obtained with BTEE had a diameter between 50 and 220 nm, with a zeta potential value of −20 mV at pH 4. The pKa of tyrosine oligomers is around 7, meaning that the BTEE oligomers were present in their ionized form, conferring to the nanoparticles, a negatively charged surface, which provided a colloidal stability.

As mentioned before, the reaction depends upon the hydrophobicity, surface activity, and concentration of the solute molecule. The surface activity of solute molecules can depend on the ionic strength of the solution. The BTEE due to its high hydrophobicity was easy to get adsorb at bubble surface even the reaction was carried out in the water. In case of phenol, the formation of dimers and oligomers was reduced by 83% when reaction was performed in water instead of PBS solution. This was due to the fact that surface activity of the phenol can be enhanced in the salt solutions [55]. The salt tends to lower the surface tension allowing more phenol moieties to reach the bubble surface to yield dimers, trimers, and oligomers. Further with phenol higher concentration of 10 mM was required to form nanoparticles with size ranging between 90 and 150 nm.

The authors indicated that the nanoparticles obtained from BTEE and phenol dissolved completely in alkaline solutions (pH > 10). Additionally, they speculated that the driving force behind the phenol and BTEE oligomer assembly is the π–π stacking interactions between the aromatic rings of the moieties. This hypothesis was confirmed by fluorescence analysis of the nanoparticles before and after dissolution (Fig. 3.7).

The fluorescence emission of the phenol and BTEE nanoparticles in the range of 340–500 nm (Fig. 3.7b) was similar to that of the soluble phenol and BTEE oligomers observed in Fig. 3.5a and 3.6a, respectively. However, an additional emission of the

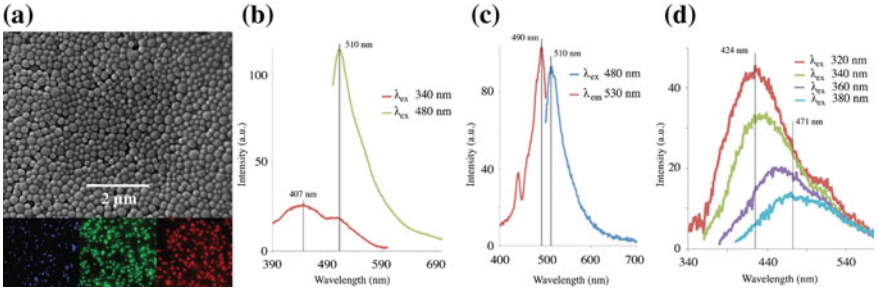

Fig. 3.7 Optical microscopy (**a**) and fluorescence properties of oligomeric nanoparticles; Fluorescence emission (**b**) and excitation (**c**) spectra of BTTE oligomeric nanoparticles and fluorescence emission spectra (**d**) of BTTE oligomeric nanoparticles after dissolution in alkaline solution. Reproduced from [40] with permission from The Royal Society of Chemistry

Table 3.1 Antioxidant activity of ascorbic acid (taken as 100%), BTEE NPs, and BTEE not treated

Compound	Antioxidant activity, Relative %
Ascorbic acid	100
BTEE NPs	56
BTEE not treated	3
Blank	0

Reproduced from [40] with permission from The Royal Society of Chemistry

BTEE nanoparticles was observed in the range of 500–700 nm when excited at 480 nm, with a maximum at 510 nm (Fig. 3.7c), and phenol nanoparticles were observed at 588 and 668 nm when excited at 540 and 600 nm [49]. The fluorescence microscopy images shown in Fig. 3.7a confirmed the generation by the nanoparticles of blue, green, and red emissions. After dissolution in alkaline solution (Fig. 3.7d), this new band disappeared, while the fluorescence observed was typical of soluble phenol and BTEE oligomers (Fig. 3.7d). Phenol also exhibited the same behavior in alkaline solution [49]. This again provides evidence for π–π stacking interaction between the aromatic phenolate moieties of oligomers, which can reduce the ground- and excited-state energy leading to new redshifted emissive bands. This has been observed in green fluorescent proteins (GFP) where their green fluorescence was redshifted [56]. The observed redshift was attributed to the π–π stacking interactions between the phenolate anion and different moieties with aromatic rings [56].

The antioxidant properties of the BTEE oligomers nanoparticles were tested against the antioxidant properties of ascorbic acid, using an assay based on DPPH radical reduction (Table 3.1).

Compared to untreated BTEE, the nanoparticles produced by Cavalieri et al. demonstrated a strong antioxidant activity, which was attributed to the extensive hydroxylation of conjugated rings. Similarly, the antioxidant activity of the sonicated phenol was more than 50% as compared to the phenol which did not show any radical scavenging activity (Fig. 3.8a). Also shown is the proposed mechanism of the radical scavenging by hydroxylated phenolic dimers (Fig. 3.8b).

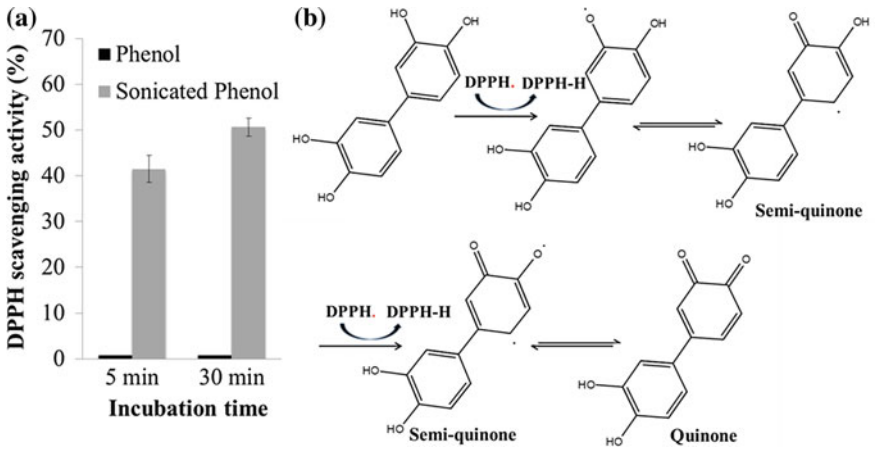

Fig. 3.8 **a** Percentage DPPH scavenging activity of sonicated phenol and phenol after 2 min and 30 min. **b** The proposed mechanism for the oxidation of phenolic dimer by DPPH radical. Reproduced with permission from [49], Copyright 2016 American Chemical Society

The authors then extended this study to complex protein systems such as lysozyme and BSA (bovine serum albumin).

Sonication of BSA for 3 h produced a turbid solution. The authors analyzed the BSA solution via SEM analysis and performed SDS analysis for both lysozyme and BSA to evaluate if covalent bonds were generated also inter-molecularly (Fig. 3.9).

The results showed the formation of higher molecular weight for both lysozyme and BSA, signifying that the dimerization of tyrosine not only occurred intra-molecularly but also inter-molecularly. When BSA was utilized, the formation of nanoparticles with a mean diameter of about 150 nm, and emitting in the blue and red region, was observed.

Recently, this strategy (high-frequency ultrasonication) was also applied for the conversion of tannic acid to ellagic acid [57]. Tannic acid is naturally occurring polyphenol which consists of D-glucopyranose as a central core attached to multiple galloyl and gallic acid units [58, 59]. Both ellagic acid and tannic acid are found to have different applications in biomedicine and food [60–62]. The ellagic acid is mostly obtained by enzymatic hydrolysis of the ellagitannins [63, 64] or multistep organic reactions [65] with no control over size and shape. Bhangu et al. have used high-frequency ultrasound to produce ellagic acid and its derivatives from tannic acid [57]. The formation of ellagic acid and other products was confirmed by HPLC, ^{1}H and ^{13}C NMR, mass, and absorption spectroscopies. Scheme 3.2 shows the proposed mechanism for the conversion of tannic acid to ellagic acid and its derivative by high-frequency ultrasound. The ultrasonically generated shear stresses and radicals led to the hydrolysis of the galloyl moieties present in the tannic acid as shown in step 1 (Scheme 3.2). Usually, such conversion requires very long time and use of acid or base catalyst. The formation of gallic acid was confirmed by HPLC. Then, step

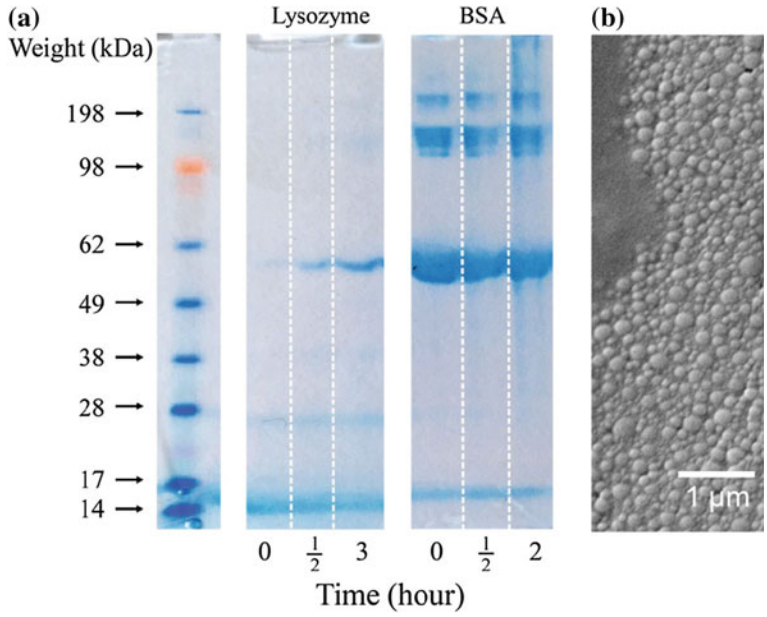

Fig. 3.9 **a** SDS PAGE gel of sonicated lysozyme and BSA, **b** SEM image of BSA

2 gallic acid units combined to form gallic acid dimers through C–C coupling by the similar mechanism as described previously with BTEE and phenol (Scheme 3.1). Finally, gallic acid undergoes spontaneous lactonization to form ellagic acid (step 3).

Therefore, high-frequency ultrasound in this case can be used to perform multiple reactions such as hydrolysis of ester linkage, oxidative coupling of phenolic moieties, and crystallization of product with controlled shape and size. The change in the size and shape of the crystals obtained can be noted in Fig. 3.10. Particles obtained were having different morphologies depending on the concentration of TA, frequency, power, and time of sonication. With the change in the initial concentration of tannic acid from 0.5 mM (Fig. 3.10a) to 1 mM (Fig. 3.10b), size increased from 3.7 to 7 μm and morphology changed from small discoidal to large flat ellipsoidal. Similarly, by switching frequency from 355 to 1 MHz at 5.5 W/cm^3 and power from 5 to 20 W/cm^3 at 355 kHz, the size was reduced from 7 to 9.5 μm (Fig. 3.10 b and c) and 7 μm to 200–350 nm, respectively (Fig. 3.10d–f). Figure 3.10g and h compares the average length of crystals at different powers and frequencies. The size and distribution of crystals depend on the number and growth rate of nuclei, i.e., more the nuclei population smaller will be the size [66, 67]. With increase in the frequency, the radical yield involved in the formation ellagic acid and physical effects of ultrasound decreases. So, the nucleation rate decreases and as it is inversely related to size, the size rises.

On the contrary, with an increase in the ultrasonic power, the effect is opposite as the radical yield is higher and physical effects such as shear stresses, turbulence,

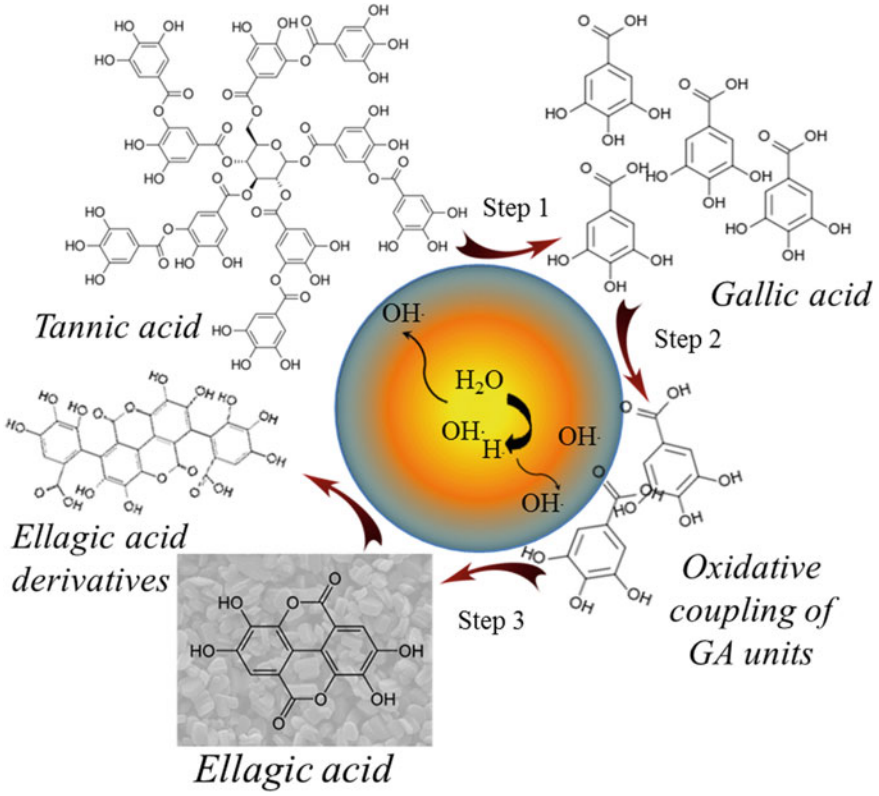

Scheme 3.2 Schematic of the proposed mechanism for the formation of ellagic acid and its derivatives from tannic acid by sonication. Reproduced from [57] with permission from The Royal Society of Chemistry

microjetting, etc. are also enhanced. This would improve the local supersaturation significantly as higher amount of ellagic acid is produced resulting in enhancement of rate of nucleation and decrease in crystal size.

Apart from this, the particles synthesized were found to have high colloidal stability, thermostablity as compared to tannic acid. The particles were found to be fluorescent in blue, green, and red region as observed from fluorescence emission spectra (Fig. 3.11a) and fluorescence microscopic images (Fig. 3.11b). The antioxidant activity of the ellagic acid crystals produced by ultrasound was slightly higher than that of commercially ellagic acid at all the concentrations (Fig. 3.11c). The antioxidant activity can help to protect the cells against any damage from the free radicals. Different polyphenolic molecules have been proven to have anticancer activity due to their tendency to reduce proliferation by inducing apoptosis [68]. The anticarcinogenic

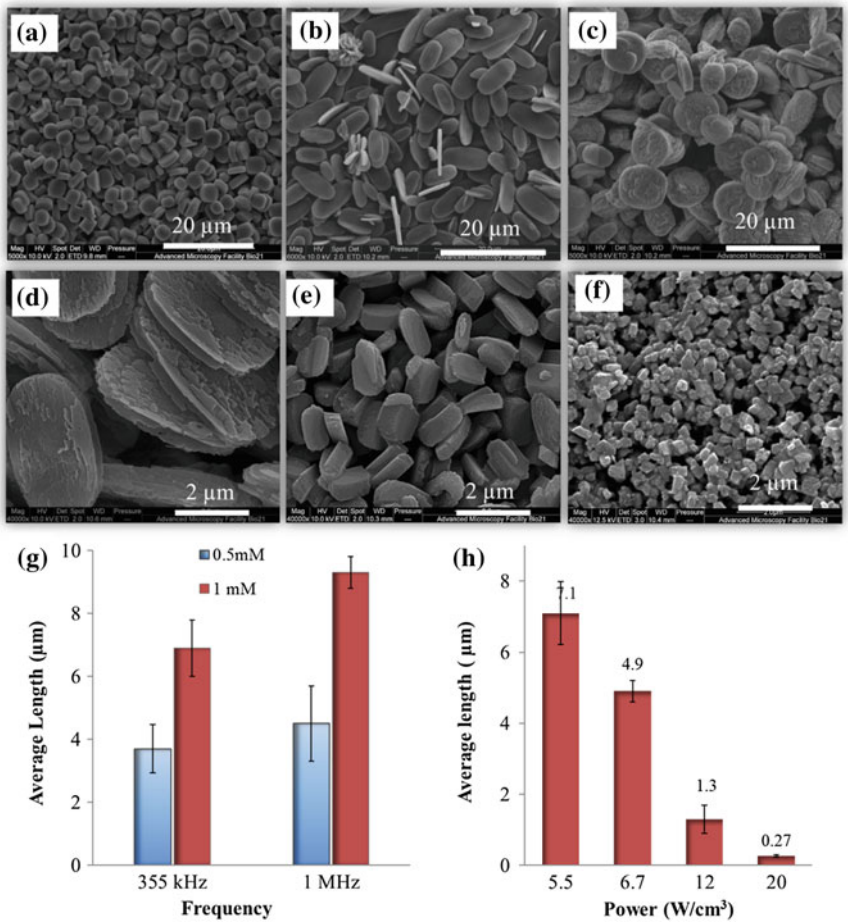

Fig. 3.10 SEM images of the TAS crystals **a** and **b** with 0.5 mM and 1 mM TA, respectively, at 355 kHz 5.5 W/cm^3; **c** TA 1 mM 1 MHz 5.5 W/cm^3; **d**, **e**, **f** 1 mM TA 355 kHz at power 6.7, 12, 20 W/cm^3, respectively. **g** Average length of TAS crystals at different frequencies and concentrations of TA; and **h** dependence of average length of TAS crystals at different ultrasonic powers. Reproduced from [57] with permission from The Royal Society of Chemistry

activity of ultrasonically generated ellagic acid particles was higher than the tannic acid at all concentration toward MDA-MB-231 breast cancer cells after 24 h as shown in Fig. 3.11d. If the IC_{50} value is considered, TAS particle has 20 to 10 µg/ml, whereas TA has > 0 µg/ml (Fig. 3.11d). The anticancer activity of ellagic acid moieties in solution toward MDA-MB-231 breast cancer cells has been reported many times [68, 69]. The ellagic acid lead to the inhibition of cell proliferation along with that it can help in the migration of cells through VEGF-induced angiogenesis, VEGF-2 tyro-

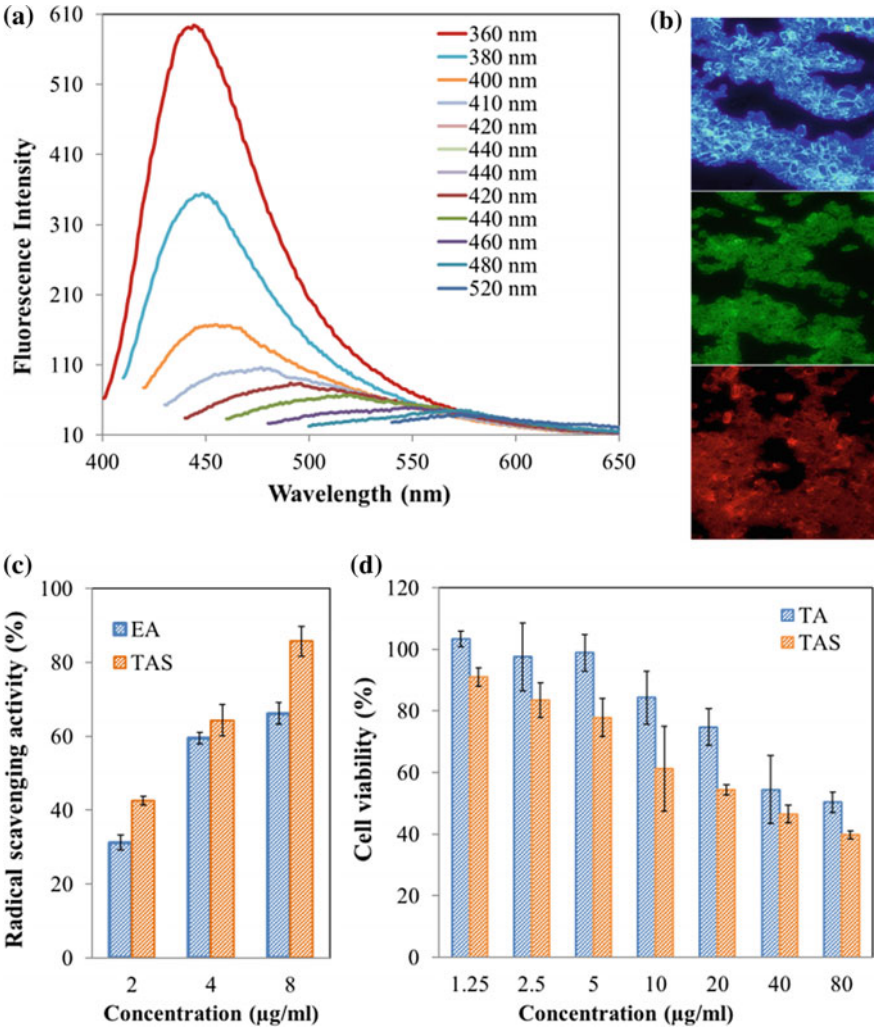

Fig. 3.11 **a** Fluorescence emission spectra of TAS particles after dissolution at different excitation wavelengths, **b** Fluorescence microscopic images of the TAS particles, **c** Percentage radical scavenging activity of ellagic acid and TAs particles after 3 min incubation with DPPH solution as a function of concentrations, and (d) Cell viability of TA and TAS after 24 h at different concentrations toward MDA-MB-231 cells. Reproduced from [57] with permission from The Royal Society of Chemistry

sine kinase activity and its downstream MAPK, and PI3 K/Akt pathways [69, 70]. Consequently, this formation of tannic acid can be utilized to treat breast cancer cells and the activity can be further enhanced by loaded hydrophobic drugs to the particles.

In summary, it has been discussed in this review that the reactive and oscillating surface of cavitation microbubbles acts as a catalytic binding site for the dimeriza-

tion and oligomerization of different biomolecules bearing phenolic moieties such as polyphenols, aromatic amino acids, etc. at the gas–liquid interface. The ultrasonic oxidation of these moieties bearing biomolecules results in the formation of fluorescent dimers and oligomers, which could self-assemble in highly fluorescent and antioxidant nanoparticles. These nanoparticles may find application in several fields, such as antioxidant, anticancer, and imaging agents. Additionally, the authors illustrated a single-step controlled ultrasonic approach as a strategy for the fabrication of these nanoparticles, without using external oxidants, inorganic catalysts, or enzymes. Another strength of this study lies in the avoidance of complicated preparation steps and in the absence of potential dangerous or toxic agents.

References

1. R.M. Fitch, C. Tsai, Polymer colloids: particle formation in nonmicellar systems. J. Polym. Sci., Part C: Polym. Lett. **8**(10), 703–710 (1970)
2. G. Cooper, F. Grieser, S. Biggs, Butyl acrylate/vinyl acetate copolymer latex synthesis using ultrasound as an initiator. J. Colloid Interface Sci. **184**(1), 52–63 (1996)
3. P. Kruus, D. McDonald, T. Patraboy, Polymerization of styrene initiated by ultrasonic cavitation. J. Phys. Chem. **91**(11), 3041–3047 (1987)
4. S. Biggs, F. Grieser, Preparation of polystyrene latex with ultrasonic initiation. Macromolecules **28**(14), 4877–4882 (1995)
5. S.K. Ooi, S. Biggs, Ultrasonic initiation of polystyrene latex synthesis. Ultrason. Sonochem. **7**(3), 125–133 (2000)
6. J. Zhang, Y. Cao, Y. He, Ultrasonically irradiated emulsion polymerization of styrene in the presence of a polymeric surfactant. J. Appl. Polym. Sci. **94**(2), 763–768 (2004)
7. Y. He, Y. Cao, Y. Fan, Using anionic polymerizable surfactants in ultrasonically irradiated emulsion polymerization to prepare polymer nanoparticles. J. Appl. Polym. Sci. **107**(3), 2022–2027 (2008)
8. Y. He, Y. Cao, Y. Liu, Initiation mechanism of ultrasonically irradiated emulsion polymerization. J. Polym. Sci., Part B: Polym. Phys. **43**(18), 2617–2624 (2005)
9. M.A. Bradley et al., Miniemulsion copolymerization of methyl methacrylate and butyl acrylate by ultrasonic initiation. Macromolecules **38**(15), 6346–6351 (2005)
10. H. Xia, Q. Wang, G. Qiu, Polymer-encapsulated carbon nanotubes prepared through ultrasonically initiated in situ emulsion polymerization. Chem. Mater. **15**(20), 3879–3886 (2003)
11. M. Bradley, F. Grieser, Emulsion polymerization synthesis of cationic polymer latex in an ultrasonic field. J. Colloid Interface Sci. **251**(1), 78–84 (2002)
12. F. Cavalieri et al., One-pot ultrasonic synthesis of multifunctional microbubbles and microcapsules using synthetic thiolated macromolecules. Chem. Commun. **47**(14), 4096–4098 (2011)
13. F. Cavalieri et al., Ultrasonic synthesis of stable, functional lysozyme microbubbles. Langmuir **24**(18), 10078–10083 (2008)
14. F. Cavalieri et al., Influence of the Morphology of Lysozyme-Shelled Microparticles on the Cellular Association, Uptake, and Degradation in Human Breast Adenocarcinoma Cells. Part. Part. Syst. Charact. **30**(8), 695–705 (2013)
15. M. Zhou, F. Cavalieri, M. Ashokkumar, Tailoring the properties of ultrasonically synthesised microbubbles. Soft Matter **7**(2), 623–630 (2011)
16. T.D. Tran et al., Clinical applications of perfluorocarbon nanoparticles for molecular imaging and targeted therapeutics. Int. J. Nanomed. **2**(4), 515 (2007)
17. Y. Mine, F. Ma, S. Lauriau, Antimicrobial peptides released by enzymatic hydrolysis of hen egg white lysozyme. J. Agric. Food Chem. **52**(5), 1088–1094 (2004)

18. D. Cosgrove, C. Harvey, Clinical uses of microbubbles in diagnosis and treatment. Med. Biol. Eng. Compu. **47**(8), 813–826 (2009)
19. K. Ferrara, R. Pollard, M. Borden, Ultrasound microbubble contrast agents: fundamentals and application to gene and drug delivery. Annu. Rev. Biomed. Eng. **9**, 415–447 (2007)
20. M. Postema, Medical bubbles. Med. Phys. **32**(5), 1450 (2005)
21. P. Morse, K. Ingard, *Theoretical Acoustics* (McGrawHill, New York, 1968), Google Scholar: pp. 252–255
22. S.H. Bloch et al., Optical observation of lipid-and polymer-shelled ultrasound microbubble contrast agents. Appl. Phys. Lett. **84**(4), 631–633 (2004)
23. N. de Jong et al., Absorption and scatter of encapsulated gas filled microspheres: theoretical considerations and some measurements. Ultrasonics **30**(2), 95–103 (1992)
24. N. de Jong, L. Hoff, Ultrasound scattering properties of Albunex microspheres. Ultrasonics **31**(3), 175–181 (1993)
25. W.-S. Chen et al., A comparison of the fragmentation thresholds and inertial cavitation doses of different ultrasound contrast agents. J. Acoust. Soc. Am. **113**(1), 643–651 (2003)
26. F. Cavalieri et al., Antimicrobial and biosensing ultrasound-responsive lysozyme-shelled microbubbles. ACS Appl. Mater. Interfaces **5**(2), 464–471 (2013)
27. S. Chapalamadugu, G.R. Chaudhry, Microbiological and biotechnological aspects of metabolism of carbamates and organophosphates. Crit. Rev. Biotechnol. **12**(5–6), 357–389 (1992)
28. M.S. Ayyagari et al., Controlled free-radical polymerization of phenol derivatives by enzyme-catalyzed reactions in organic solvents. Macromolecules **28**(15), 5192–5197 (1995)
29. A. Nozoe et al., Germanium recovery using polyphenol microspheres prepared by horseradish peroxidase reaction. J. Chem. Technol. Biotechnol. **86**(11), 1374–1378 (2011)
30. B. Eker et al., Enzymatic polymerization of phenols in room-temperature ionic liquids. J. Mol. Catal. B Enzym. **59**(1), 177–184 (2009)
31. S. Dubey, D. Singh, R. Misra, Enzymatic synthesis and various properties of poly (catechol). Enzyme Microb. Technol. **23**(7), 432–437 (1998)
32. F.F. Bruno et al., Novel enzymatic polyethylene oxide-polyphenol system for ionic conductivity. J. Macromol. Sci. Part A **39**(10), 1061–1068 (2002)
33. Y.-J. Kim, H. Uyama, S. Kobayashi, Regioselective synthesis of poly (phenylene) as a complex with poly (ethylene glycol) by template polymerization of phenol in water. Macromolecules **36**(14), 5058–5060 (2003)
34. Y.J. Kim, H. Uyama, S. Kobayashi, Peroxidase-catalyzed oxidative polymerization of phenol with a nonionic polymer surfactant template in water. Macromol. Biosci. **4**(5), 497–502 (2004)
35. T. Heck et al., Enzyme-catalyzed protein crosslinking. Appl. Microbiol. Biotechnol. **97**(2), 461–475 (2013)
36. Z. Chen et al., Biocompatible, functional spheres based on oxidative coupling assembly of green tea polyphenols. J. Am. Chem. Soc. **135**(11), 4179–4182 (2013)
37. J. Fei et al., One-pot ultrafast self-assembly of autofluorescent polyphenol-based core@ shell nanostructures and their selective antibacterial applications. ACS Nano **8**(8), 8529–8536 (2014)
38. C. Houée-Lévin et al., Exploring oxidative modifications of tyrosine: an update on mechanisms of formation, advances in analysis and biological consequences. Free Radical Res. **49**(4), 347–373 (2015)
39. T. Michon et al., Horseradish peroxidase oxidation of tyrosine-containing peptides and their subsequent polymerization: a kinetic study. Biochemistry **36**(28), 8504–8513 (1997)
40. F. Cavalieri et al., Sono-assembly of nanostructures via tyrosine–tyrosine coupling reactions at the interface of acoustic cavitation bubbles. Materials Horizons **3**, 563–567 (2016)
41. M. Ashokkumar, T.J. Mason, *S*onochemistry. Kirk-Othmer Encycl. Chem. Technol. y On-Line, Wiley Interscience (2007)
42. J. Berthelot, Y. Benammar, C. Lange, A mild and efficient sonochemical bromination of alkenes using tetrabutylammonium tribromide. Tetrahedron Lett. **32**(33), 4135–4136 (1991)
43. S.K. Bhangu, M. Ashokkumar, Theory of sonochemistry. Top. Curr. Chem. **374**(4), 56 (2016)
44. M.H. Entezari, C. Pétrier, A combination of ultrasound and oxidative enzyme: sono-enzyme degradation of phenols in a mixture. Ultrason. Sonochem. **12**(4), 283–288 (2005)

45. S. Okouchi, O. Nojima, T. Arai, Cavitation-induced degradation of phenol by ultrasound. Water Sci. Technol. **26**(9–11), 2053–2056 (1992)
46. C. Petrier et al., Sonochemical degradation of phenol in dilute aqueous solutions: comparison of the reaction rates at 20 and 487 kHz. J. Phys. Chem. **98**(41), 10514–10520 (1994)
47. N. Serpone et al., Sonochemical oxidation of phenol and three of its intermediate products in aqueous media: catechol, hydroquinone, and benzoquinone. Kinetic and mechanistic aspects. Res. Chem. Intermed. **18**(2), 183–202 (1992)
48. C. Wu et al., Photosonochemical degradation of phenol in water. Water Res. **35**(16), 3927–3933 (2001)
49. S.K. Bhangu, M. Ashokkumar, F. Cavalieri, A simple one-step ultrasonic route to synthesize antioxidant molecules and fluorescent nanoparticles from phenol and phenol-like molecules. ACS Sustain. Chem. Eng. **5**(7), 6081–6089 (2017)
50. F.F. Bruno et al., Polymerization of water-soluble conductive polyphenol using horseradish peroxidase. J. Macromol. Sci. Part A **38**(12), 1417–1426 (2001)
51. P.K. Jha, G.P. Halada, The catalytic role of uranyl in formation of polycatechol complexes. Chem. Cent. J. **5**(1), 12 (2011)
52. D.A. Malencik et al., Dityrosine: preparation, isolation, and analysis. Anal. Biochem. **242**(2), 202–213 (1996)
53. G.J. Smith, T.G. Haskell, The fluorescent oxidation products of dihydroxyphenylalanine and its esters. J. Photochem. Photobiol., B **55**(2), 103–108 (2000)
54. J. Chandrapala et al., Effects of ultrasound on the thermal and structural characteristics of proteins in reconstituted whey protein concentrate. Ultrason. Sonochem. **18**(5), 951–957 (2011)
55. A.K. Goard, E.K. Rideal, CCXXI—The surface tensions of aqueous phenol solutions. Part II. Activity and surface tension. J. Chem. Soc. Trans. **127**, 1668–1676 (1925)
56. R.Y. Tsien, The green fluorescent protein. Annu. Rev. Biochem. **67**(1), 509–544 (1998)
57. S.K. Bhangu et al., Sono-transformation of tannic acid into biofunctional ellagic acid micro/nanocrystals with distinct morphologies. Green Chem. **20**, 816–821 (2018)
58. I. Mueller-Harvey, Analysis of hydrolysable tannins. Anim. Feed Sci. Technol. **91**(1), 3–20 (2001)
59. L. Pouységu et al., Synthesis of ellagitannin natural products. Nat. Prod. Rep. **28**(5), 853–874 (2011)
60. H. Ejima et al., One-step assembly of coordination complexes for versatile film and particle engineering. Science **341**(6142), 154–157 (2013)
61. S. Quideau et al., Plant polyphenols: chemical properties, biological activities, and synthesis. Angew. Chem. Int. Ed. **50**(3), 586–621 (2011)
62. N. Bertleff-Zieschang et al., Biofunctional metal–phenolic films from dietary flavonoids. Chem. Commun. **53**(6), 1068–1071 (2017)
63. A. Brune, B. Schink, Phloroglucinol pathway in the strictly anaerobic Pelobacter acidigallici: fermentation of trihydroxybenzenes to acetate via triacetic acid. Arch. Microbiol. **157**(5), 417–424 (1992)
64. L. Mingshu et al., Biodegradation of gallotannins and ellagitannins. J. Basic Microbiol. **46**(1), 68–84 (2006)
65. Q. Sun, J. Heilmann, B. König, Natural phenolic metabolites with anti-angiogenic properties–a review from the chemical point of view. Beilstein J. Org. Chem. **11**, 249 (2015)
66. S. Kaur Bhangu, M. Ashokkumar, J. Lee, Ultrasound assisted crystallization of paracetamol: crystal size distribution and polymorph control. Cryst. Growth Des. **16**(4), 1934–1941 (2016)
67. V.S. Nalajala, V.S. Moholkar, Investigations in the physical mechanism of sonocrystallization. Ultrason. Sonochem. **18**(1), 345–355 (2011)
68. H.-M. Zhang et al., Research progress on the anticarcinogenic actions and mechanisms of ellagic acid. Cancer Biol. Med. **11**(2), 92 (2014)
69. N. Wang et al., Ellagic acid, a phenolic compound, exerts anti-angiogenesis effects via VEGFR-2 signaling pathway in breast cancer. Breast Cancer Res. Treat. **134**(3), 943–955 (2012)
70. L. Tang et al., Inhibition of angiogenesis and invasion by DMBT is mediated by downregulation of VEGF and MMP-9 through Akt pathway in MDA-MB-231 breast cancer cells. Food Chem. Toxicol. **56**, 204–213 (2013)